VNU Journal of Science: Comp. Science & Com. Eng., Vol. 42, No. xx (2026) xx–xx

VNU Journal of Science:
Computer Science and Communication Engineering

Journal homepage: http://www.jcsce.vnu.edu.vn/index.php/jcsce

Review Article

Ray-Tracing Channel Models for Near-Field Communication

Nguyen The Khang[1], Do Hai Son[2], Tran Trong Duy[3], Thanh Trung Le[1], Tran Thi Thuy Quynh[1], Karim Abed-Meraim[4], Merouane Debbah[5], Nguyen Linh Trung[1*]

[1] *VNU University of Engineering and Technology, Hanoi, Vietnam*
[2] *School of Electrical Engineering, Computing and Mathematical Sciences, Curtin University, Australia*
[3] *CentraleSupélec, Université Paris-Saclay, CNRS, L2S, Gif-sur-Yvette, France*
[4] *PRISME Laboratory (IUF member), University of Orléans, Orléans, France*
[5] *Khalifa University, Abu Dhabi, United Arab Emirates*

Received 18th March 2026
Revised 27th March 2026; Accepted 13th May 2026

Abstract: Extremely large-scale multiple-input multiple-output (XL-MIMO) and Terahertz-band communications (THz) are widely considered as key potential enabling technologies for sixth-generation (6G) wireless networks to achieve their ambitious performance targets. Those advanced technologies induce a paradigm shift in the electromagnetic characteristics, such as a significant expansion of the near-field region, thereby redefining the 6G propagation model. The intrinsic differences between near-field and far-field wave propagation models introduce new challenges for near-field communications (NFC), particularly in accurately characterizing the underlying channel's properties. This article begins with an investigation into the complex phenomena induced by 6G enabling technologies and distinctive electromagnetic regions. We then provide rigorous derivations of ray-tracing channel models for two widely adopted antenna array architectures, explicitly accounting for the unique propagation characteristics of radiating near-field regions, and also contrast them with the ongoing 3GPP standardization efforts. We also conduct a systematic review of the channel models used in recent progress in channel estimation, and align them with our presented models. Finally, we offer an overview that addresses key challenges and highlights emerging opportunities for NFC within the 6G paradigm.

Keywords: XL-MIMO, 6G, near-field communications, ray-tracing channel models.

*Corresponding author.
E-mail address: linhtrung@vnu.edu.vn

https://doi.org/10.25073/2588-1086/vnucsce.7077

1. Introduction

Sixth-generation (6G) networks promise to reshape our interaction with the digital world through transformative applications like extended reality, holographic communications, and the Metaverse [1–4]. These services impose stringent requirements far beyond prior generations [5, 6], as summarized in Table 1: a tenfold improvement in spectral efficiency, peak data rates reaching 1 Tbps, massive connection density, ubiquitous coverage, and sub-millisecond latency [7, 8]. A common driver for these targets is the move toward extremely large antenna apertures and higher frequency bands, which paves the way for a fundamental shift in electromagnetic characteristics [8, 9]. The emergence of XL-MIMO and THz will consequently push wireless communication systems to the near-field region, requiring new propagation models beyond the conventional far-field regime [4, 10].

Table 1. Key Performance Indicators (KPIs) for 5G versus 6G wireless networks

KPIs for network	**5G**	**6G**
Spectral efficiency	0.1 kbps/Hz	1 kbps/Hz
Peak data rate	20 Gbps	1 Tbps
Coverage	7%	90%
Access density	1 user/m^2	100 users/m^2
Latency	2 ms	0.5 ms

1.1. XL-MIMO & THz

Multiple-input multiple-output (MIMO) communication was introduced in 4G LTE networks to enhance data rate capacity [11]. Since then, it has evolved into a cornerstone of 5G through massive MIMO (mMIMO), and is advancing further in 6G with XL-MIMO to meet its superior demands. Similar to the concept of mMIMO, the basic idea of XL-MIMO is to deploy a tremendous number of antennas in a compact space, offering significant enhancements in spectral efficiency and spatial resolution [12]. This scaling trend can be summarized in Table 2, which highlights the key distinctions between conventional mMIMO and emerging XL-MIMO architectures.

Table 2. Comparison between mMIMO and XL-MIMO systems

Metric	**mMIMO**	**XL-MIMO**
Number of antennas	64–256	1000+
Array aperture	Moderate	Large
Beam gain	High	Higher
Precoding complexity	High	Higher
Beam management	Difficult	Very difficult
Power consumption	High	Higher

Prior work on MIMO implementation has primarily relied on spatially discrete antennas (SPD), typically deployed with half-wavelength spacing. In contrast, a more advanced paradigm exploits meta-material technology to embed an extremely dense array of infinitesimal antennas across a continuous surface, a concept referred to as continuous aperture MIMO (CAP-MIMO). Although this novel antenna can realize the near-optimal beamforming, it also introduces substantial hardware and computational complexity [12]. Hence, the focus of this article is restricted to SPD-based XL-MIMO implementations, typically realized through extremely large antenna arrays (ELAA), while CAP-MIMO is acknowledged as a promising future direction.

Spanning the radio-frequency spectrum from 300 GHz to 10 THz, the THz band bridges the gap between microwave and optical frequencies. It complements millimeter wave (mmWave) communication and visible light communication by providing quasi-optical paths that offer both Tbps-level data rate and robust behavior to environmental factors like atmospheric turbulence and fog [13].

Despite this potential, THz communication faces two primary challenges. First, severe propagation losses and power limitations

necessitate the integration of ELAA systems to maintain short-range connectivity [13, 14]. Second, the significant computational burden at the digital baseband requires innovative solutions. However, the inherent sparsity of THz channels allows for the effective use of compressed sensing [13]. Furthermore, the transition to high-frequency, large-scale antenna arrays shifts many scenarios into the near-field region, introducing different types of complexity, such as spatial nonstationarity and beam splitting [15].

1.2. 6G Empowers NFC

According to electromagnetic and antenna theory, the field surrounding a base station is divided into near-field (NF) and far-field (FF) regions, with the boundary between them defined by the Rayleigh distance [16, 17]. This distance is a value proportional to the square of the antenna aperture D and the carrier frequency f_c, and is defined as

$$R_D = \frac{2D^2}{\lambda_c} = \frac{2N^2 d^2 f_c}{c}, \tag{1}$$

where c is the light speed and for a uniform linear array with $N+1$ antenna elements of inter-element spacing d, the aperture is $D = Nd$.

From first-generation (1G) networks to 5G mMIMO systems, the moderate apertures and frequencies typically limited R_D to only a few meters, making NF effects negligible. However, the 6G paradigm, driven by the scaling of antenna arrays and the shift toward higher frequency bands, substantially extends this distance, putting NF communication (NFC) under the spotlight [7–9]. In an experiment conducted in [18], an ELAA, prototyped with 3,200 elements, achieved an NF limit of 200 meters at 2.4 GHz, and thus would place the majority of user devices within the NF region.

Recent studies have revealed that 6G networks can substantially benefit from the NF propagation. Under the spherical wavefront assumption, a free-space line-of-sight (LoS) channel can achieve significantly enhanced spatial degrees of freedom (DoF), as its channel matrix exhibits higher rank compared to the rank-one counterpart in the FF [19, 20]. Moreover, NF propagation enhances multi-user accessibility by exploiting spherical wavefronts to generate spatially focused beams [21, 22], enabling simultaneous service to users at different positions through location-division multiple access (LDMA) [23–25]. The key distinction between NF and FF propagation lies in the wavefront representation. This difference not only alters the mathematical structure of the channel but also transforms core signal processing principles, i.e., particularly beamforming, realized as the capability of directing a signal toward a specific region of interest rather than broadcasting it in all directions [21].

Hence, the failure in capturing these unique characteristics can lead to severe model mismatches that undermine the potential of NFC applied for signal processing tasks in 6G, such as channel estimation, localization, and sensing. Accurate NF channel models are therefore critical as a reliable foundation to evaluate and unleash the prospects of 6G-NFC.

1.3. Related Works

Channel modeling approaches are broadly categorized into deterministic ray-tracing models and stochastic geometry-based models [38, 39]. Unlike deterministic models, which require precise knowledge of environmental geometry and scattering propagation, stochastic approaches rely on probabilistic distributions to characterize propagation uncertainty [40]. This abstraction may yield significant computational efficiency and analytical tractability for general performance analysis [41, 42]. However, developing statistical channel models that accurately reflect the NF regime remains an open challenge; the difficulties lie in capturing complex environmental dynamics, such as scattering and reflections,

Table 3. Recent contributions on NF channel models for 6G systems

Category	Reference	Model	Key Contributions
Foundation survey on NF	[26] -2023	-	Present a comprehensive exploration of NFC versus FFC across four key paradigms, then highlight how spherical wavefront-based NFC distinguishes itself from conventional far-field FFC.
	[27] -2022	-	Highlight the non-linear phase of spherical waves and derive near-field boundary, discuss key challenges and reveal potentials of NFC for 6G in enhancing capacity and accessibility.
THz models	[28] -2022	-	Provide valuable insights of THz band propagation models, and identify the recent efforts to establish evaluation metrics for 6G applications along with THz.
6G GBSMs Foundation	[29] -2022	Geo	Propose a pervasive wireless channel modeling theory, and construct an unified statistical modeling framework that integrate important channel characteristics at different frequency bands and scenarios.
XL-MIMO schematics	[30] -2023	Ray	Present four XL-MIMO architectures from a hardware viewpoint, and discuss about the challenges and opportunities in channel modeling, performance analysis, and signal processing tasks.
	[31] -2024	Ray	Present comprehensive channel models for general array geometries of XL-MIMO with an emphasis on performance analysis, practical design issues, and promising directions for future work.
Near-field Channel Models	[32] -2024	Ray	Provide a detailed overview of near-field channel models for SPD and CAP antenna arrays. A particular focus is placed on the spatial nonstationarity of near-field channels.
	[33] -2024	Ray	Present an accurate modeling of general near-field channel behaviors for both SPD and CAP antennas, covering MISO/MIMO configurations with ULA and UPA.
	[15] -2024	Both	Present a comprehensive survey of recent advancements in NFC research efforts by examining the NF propagation properties, investigating NF channel in various types of models.
Channel Models of promising paradigms for 6G	[34] -2024	Geo	Present a cluster-based statistical channel model proposed for ISAC scenarios, and integrate the existing communication channel models with sensing capability by using task-specific clusters.
	[35] -2024	Ray	Propose a Hybrid ISAC channel model to effectively handle sensing and communication operation by categorizing the environment into three distinct elements: targets, clusters, and interferences.
	[36] -2024	Ray	Propose a near-field channel modeling scheme for EIT grounded in electromagnetic scattering theory, realized through the nonstationary Gaussian random fields and the field's correlation function.
	[37] -2025	Both	Conduct a comprehensive survey for six promising technologies enabling 6G, including ISAC, XL-MIMO, THz, RISs, and SAIGNs, and address open issues in 6G channel research.

Ray = ray-tracing; Geo = geometry-based.

while simultaneously exhibiting unique NF traits like spherical wavefront and spatial nonstationarity [15, 32]. Consequently, while the ray-tracing approach introduces higher computational complexity, it remains the most reliable method for capturing intricate EM phenomena. This high-fidelity modeling is essential for the rigorous analysis and evaluation of the 6G paradigm within the realm of NFC. Hence, we will focus our efforts on ray-tracing models with deterministic site-specific assumptions. Recent progress on NF has established a systematic framework progressing from fundamental EM behaviors to propagation models and applications in NFC, as summarized in Table 3. The foundation surveys in [26, 27] highlighted the impact of wavefront curvature, and identify both potentials and hurdles of NFC. The contribution of [28] lies in the precise characteristics of THz propagation models, and its related emerging topics along with THz, such as Tbps communications and THz sensing [43, 44]. Based on a geometry-based stochastic model, [29] developed a foundational theory that covers channel characteristics and coverage scenarios in the space-time-frequency domain [45]. However, this framework lacks critical NF effects.

Recent literature characterizing the unique contributions of the NF regime is further summarized in Table 3. A systematic bridge across various XL-MIMO architectures was presented in [30], which also identified low-cost designs essential for practical deployment [46, 47]. From a different perspective, Lu *et al.* [31] constructed a framework for generally distributed antenna arrays, emphasizing the dual impact of non-uniform spherical waves (NUSW) and spatial nonstationarity. Then, the survey, conducted by Liu *et al.* in [32], addressed the NF regime by focusing on spatial nonstationarity,

yet their statistical multi-path model fails to account for the spherical wavefront's contribution. In the tutorial [33], Liu *et al.* established an accurate NF model by exploiting new wavefront curvature. Nevertheless, this tutorial still lacks a consideration of the effects of spatial nonstationarity. Finally, the comprehensive survey presented in [15] investigates NF channels from the perspective of deterministic, stochastic, and electromagnetic information theory (EIT) based models. However, their work primarily focuses on reviewing the recent progress on channel models and identifying their limitations and practical solutions to attain the evolving demands of 6G in practice; but lacks the explicit framework for near-field channel models in particular cases.

The distinct characteristics of NF channels have also been explored for key 6G technologies and beyond, specifically integrated sensing and communication (ISAC) and electromagnetic information theory (EIT). Regarding ISAC, Zhang *et al.* [34] proposed a stochastic channel model that treats cluster contributions for communication and sensing independently. In contrast, Liu *et al.* [48] developed a shared-cluster framework, where identical physical scattering environments are utilized to characterize the joint propagation of sensing and communication signals. Further refining this, the hybrid ISAC channel model introduced in [35] partitions the modeling methodology into three distinct elements to handle specific operational requirements more effectively. Moving toward a rigorous analytical approach, recent research has leveraged EIT to overcome the limitations of traditional discrete models [49]. The work carried by Wan *et al.* [36] employed nonstationary Gaussian random fields within an EIT framework to characterize the NF channel with precise evaluation of enhanced DoFs [50]. Finally, the comprehensive survey conducted by Zhang *et al.* in [37] established specific modeling requirements across six major 6G advancements and also emphasized the difficulty of incorporating complex NF effects into statistical models.

The primary limitation in the literature is the absence of an explicit mathematical framework that models physical channels for different array types, propagation paths, and scattering scenarios within compact and consistent formulations. Signal processing algorithms, particularly those for channel estimation, depend heavily on accurate underlying channel properties. Furthermore, several channel estimation works [51–54] typically treated the MIMO system as an extension of the MISO case when serving multiple users. This simplification prevents them from capturing the coupling matrix, which emerges only in explicit MIMO configurations. While this coupling component is asymptotically negligible in the FF, it becomes significant in the NF and is precisely the reason why NF-LoS channels can overcome the rank-one limitation inherent to their FF counterparts. With the presence of this coupling term, the channel representation becomes more complicated, and conventional FF approach fails to accommodate this NF channel estimation. Therefore, their assumption on multi-user employing a single antenna will be exploited to effectively bypass the contribution of the coupling matrix. Furthermore, this approach will eventually undermine the potential of NFC in 6G, since this coupling matrix can exhibit the enhanced DoF of LoS channel from its mathematical representation.

1.4. Contributions & Organization

Building upon these prior studies, this work fills a critical gap by providing an explicit, unified mathematical framework for ray-tracing channel models that jointly characterize LoS and NLoS scattering paths across MISO and MIMO configurations under uniform linear and planar arrays (ULA, UPA). First, the power of this explicit model lies in its ability to enable efficient algorithm design, for example, by leveraging polar-domain sparsity, it can obtain accurate

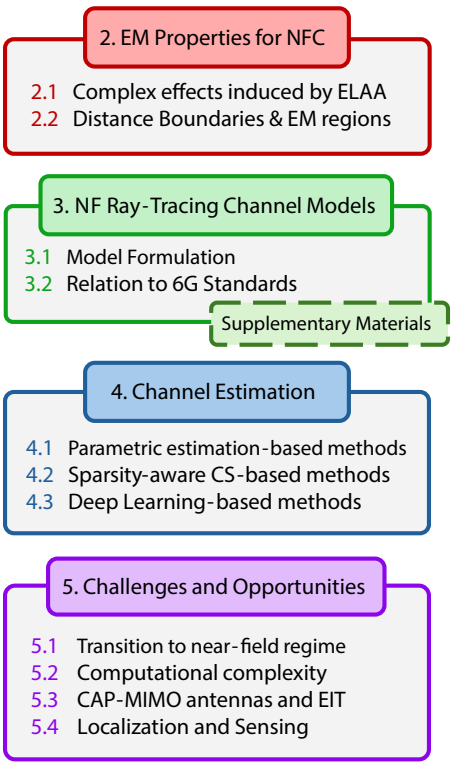

Figure 1. Condense overview for article's structure.

channel state information (CSI) with significantly reduced pilot overhead. Second, we provide a systematic survey of channel estimation research directions and examine their relationship with our presented baseline model. The surveyed works are categorized by algorithmic approaches, and their complex EM extensions.

Motivated by these needs, the main contributions of this article are summarized as depicted in Figure 1. Firstly, we begin with Section 2 by providing an overview of complex phenomena induced by a large aperture array, and clarifying the unique EM regions. In Section 3, we present the derived NF ray-tracing channel models realized through summarized final closed-form expressions, while the details will be explored thoroughly in the Appendix A.1 and further contrast these models with the 3GPP standard framework. Based on those, we provide a systematic overview of existing NF channel estimation approaches in Section 4. Finally, Section 5 offers a discussion to address the challenges and opportunities for NFC within the 6G paradigm.

Notation: Throughout this paper, scalars are denoted by italic letters. Vectors and matrices are denoted by bold-face lower- and upper-case letters, respectively. The symbol j denotes the imaginary unit, with $j^2 = -1$. The operator $\exp(\cdot)$ represents the exponential function. For a matrix $\mathbf{A}$, $[\mathbf{A}]_{m,n}$, $\mathbf{A}^{\mathsf{T}}$, $\mathbf{A}^{*}$, $\mathbf{A}^{\mathsf{H}}$, and $\|\mathbf{A}\|_{\mathrm{F}}$ denote the (m,n)-th entry, transpose, conjugate, conjugate transpose, and Frobenius norm, respectively. Then, $\mathbb{C}$ denotes the complex plane, and $\mathbb{C}^{M\times N}$ the space of $M \times N$ complex matrices. For a vector $\mathbf{a}$, $[\mathbf{a}]_i$ is the i-th entry and $\|\mathbf{a}\|$ its Euclidean norm. In spherical and cylindrical coordinate systems, position vectors are denoted by $\mathbf{r} \cdot (r, \theta, \phi)$ and $\mathbf{r} \cdot (r, \theta)$, respectively. Finally, $\otimes$ and $\odot$ denote the Kronecker and Hadamard products, respectively.

2. EM Properties for NFC

This section provides a brief overview of the electromagnetic properties of NFC in 6G. We first review the key physical phenomena induced by the usage of ELAA and THz, and recent progress to handle those. We then outline the distance boundaries that partition the radiating space into distinct regions, each accounts for the unique phase and amplitude behavior. These fundamentals provide the theoretical basis for the channel models in subsequent sections.

2.1. Complex Effects Induced by ELAA

2.1.1. Spherical Propagation Wavefront

The integration of ELAA and THz frequencies in 6G significantly expands the NF region, necessitating a shift from traditional planar wavefront modeling to a spherical wavefront assumption. Under this paradigm, signal

amplitudes and angles (AoAs/AoDs) vary across the antenna array, requiring EM traits to be characterized by both distance and angle [27]. This relationship is formally expressed as

$$\begin{aligned}\phi_n^{\text{near}}(\theta, r) &= \frac{-2\pi}{\lambda} nd\theta + \frac{(1-\theta^2)}{\lambda r}\pi n^2 d^2 \qquad (2)\\ &= \phi_n^{\text{far}}(\theta) + \phi_n^*(\theta, r),\\ \phi_n^*(\theta, r) &= \frac{(1-\theta^2)}{\lambda r}\pi n^2 d^2 \to 0 \ \text{ as } r \to \infty.\end{aligned}$$

In this context, $\phi_n^*(\theta, r)$ captures the non-linear phase variations unique to NF propagation. Because this term depends jointly on distance and angle, NF beamforming enables precise energy focusing at a specific spatial location, unlocking a new dimension of spatial multiplexing.

2.1.2. Spatial Nonstationarity and Visibility Region

Spatial stationarity occurs when an antenna array shares a uniform experience of UEs and scatterers, resulting in identically distributed power, delay, and phase across all elements. While this assumption is only held for the moderate array dimensions of prior generations, the advent of XL-MIMO introduces spatial nonstationarity. To be more specific, different segments of the array may perceive distinct perspectives of the propagation environment, leading to significant variations in radiated characteristics [55–57].

In such nonstationary environments, clusters and UEs are often visible only to specific segments of the array, a concept defined as the visibility region (VR) as depicted in Figure 2. While the VR captures the majority of the signal power, the remainder of the array is effectively "invisible" due to rapid attenuation over the massive aperture [55]. Consequently, current research often models the channel as approximately stationary within these VRs and negligible outside them. Many works have endeavored to address the spatial nonstationarity for ELAA, a common implementation of this

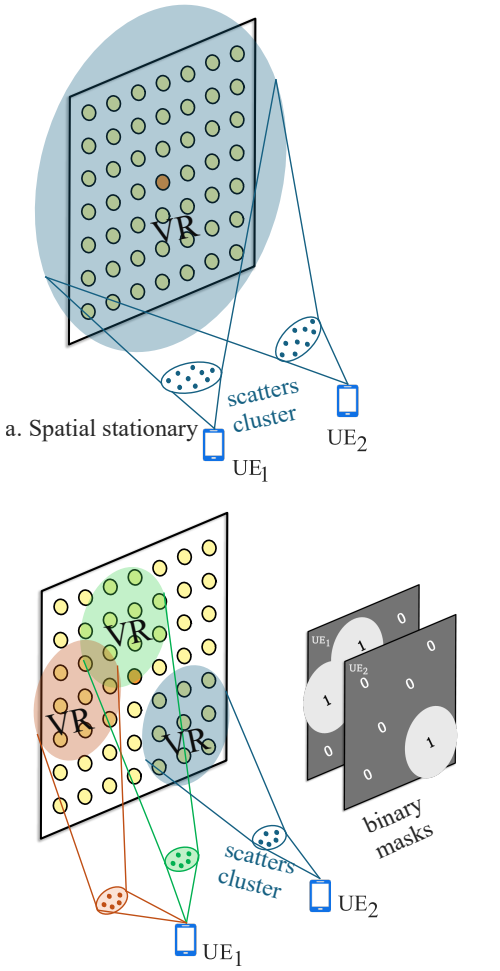

Figure 2. Visibility regions of stationary and nonstationary ELAA.

model involves applying binary masks to the array, effectively isolating the specific sub-arrays visible to the clusters of interest [57].

2.1.3. Beam Splitting in Wideband systems

Beam splitting is a critical phenomenon in wideband systems where beams at different frequencies focus on distinct physical locations, arising from the use of frequency-independent analog phase shifters across a large bandwidth [26, 33]. Unlike FF beam splitting, which only affects

angular directions, NF beam splitting accounts for both angle and distance domains [21, 58]. This misalignment will cause a severe array gain loss, since the focused energy for most subcarriers is not aligned with the user's actual location [27].

The primary solution for this is true-time delay (TTD) modules between radio-frequency (RF) chains and phase shifters, introducing additional time-delay components to enable frequency-dependent analog beamforming. However, the substantially higher power consumption of TTDs necessitates a lightweight architectural design [33]. To address NF beam splitting, Cui *et al.* [59] proposed a phase-delay focusing technique based on piece-wise FF subarray partitions, which then adopts FF-TTDs to compensate for the remaining spherical phase variations across subarrays. Despite posing challenges for data transmission, beam splitting can be exploited for NF rainbow beam training, which enables the base station to search multiple spatial locations simultaneously using different subcarriers, thereby drastically reducing beam training overhead [60].

2.1.4. Hybrid FF/NF Scenario

Hybrid-field communications, also referred to as cross-field, describes a scenario where users and scatterers are distributed across both the NF and FF regions relative to an ELAA [26, 59]. This mixed propagation regime arises in 6G ELAA systems because the larger aperture expands the NF region, making it impractical to assume that all users operate under a single propagation model.

The coexistence of both regimes introduces significant challenges for all signal processing tasks, including channel estimation [53, 61] and beam training [62, 63], since conventional methods designed for pure FF or pure NF fail to capture the mixed characteristics [64]. From a hardware perspective, hybrid FF/NF (HFN) architectures have been proposed to address these challenges. Such designs dynamically partition the ELAA into small subarrays to serve delay-sensitive FF users with low complexity, while using the larger aperture to support high data-rate NF users [33].

2.1.5. Multi-Polarization and Mutual Coupling

With the advent of ELAA, several works have revisited EM polarization, which was previously omitted for simplicity in conventional mMIMO. Multi-polarization in NFC, particularly the naturally arising tri-polarization effect, can significantly increase system capacity within a specific range [15, 65]. Exploiting this additional polarization axis enables higher data rates and improved spectral efficiency [15].

The dense packing of numerous antenna elements with sub-wavelength spacing introduces mutual coupling effects that impact both system design and performance evaluation. This coupling refers to the dependence of the induced voltage of each element on surrounding elements, which can significantly degrade the signal-to-interference-plus-noise ratio and reduce channel capacity [32]. Several studies address mutual coupling in communication models. The authors in [66] investigated mutual coupling in graphene-based THz antenna arrays, opening research directions for mitigation through material science. Meanwhile, [67] focused on optimizing communication systems under mutual coupling by developing algorithms that achieve the best possible performance given the inherent coupling constraints.

2.2. Distance Boundaries and EM Regions

The transition from FF to NF propagation is governed by multiple distance boundaries, each capturing distinct EM characteristics. As summarized in Table 4, three wave models, i.e., uniform planar wave (UPW), uniform spherical wave (USW), and non-uniform spherical wave (NUSW), describe how a signal propagates in a physical channel, which is modelled differently in those regions. These models are distinguished

Table 4. EM characteristics of different field regions

Field region	**Near-field**		**Far-field**
Categories	NUSW	USW	UPW
Linear phase	✗	✗	✓
Uniform power	✗	✓	✓

by two key metrics, i.e., the Rayleigh distance, which governs phase behavior, and the uniform-power distance (UPD), which governs amplitude variations. This section delineates the key distance boundaries that define the NF region. For the sake of analytical depth, the detailed mathematical derivations of these metrics for particular systems are explored in the Appendix A.2.

For brevity, the linear phase in Table 4 implies that it can be decomposed into a linear function of the antenna index through Taylor expansion, while the uniform amplitude indicates that all elements are assumed to receive similar power levels.

2.2.1. Rayleigh Distance

The Rayleigh distance, also known as the Fraunhofer distance, is defined as the maximum distance at which the phase discrepancy between spherical and planar wavefronts does not exceed $\pi/8$. This phase error arises from the second-order Taylor expansion term, while the first-order term accounts for the approximated FF phase. When the communication distance exceeds the Rayleigh distance, the UE is considered to be in the FF region operating under the planar wavefront assumption.

2.2.2. Fresnel Distance

In the radiated NF region, EM propagation follows a spherical wavefront. The Fresnel distance separates this region from the reactive NF, which is characterized by evanescent waves that decay exponentially with distance. The reactive region is typically negligible in practical communications scenarios, even with ELAA deployments [52].

2.2.3. Effective Rayleigh Distance

The classical Rayleigh distance is derived solely from phase error considerations. However, the work in [68] demonstrated that this metric overestimates the practical field boundary. While the classical R_D is approximately 98 m, beamforming gain only degrades noticeably below 30 m. Accordingly, the authors introduced the effective Rayleigh distance, which establishes a non-uniform NF boundary based on beamforming gain degradation. This metric is always smaller than the classical R_D and enables an alternative model for wideband beamforming based on their proposed piece-wise FF approximation [59].

2.2.4. Uniform-Power Distance

As shown in Table 4, R_D only addresses phase errors while assuming uniform amplitude across the array. The uniform-power distance (UPD) defines the boundary beyond which amplitude differences across antenna elements become negligible. UPD is determined by the minimum distance at which the power ratio between the weakest and strongest signal exceeds a given threshold [12]. Beyond UPD, all receiver antenna elements experience nearly identical signal amplitudes. This distance typically lies between the Fresnel and Rayleigh distances.

2.2.5. Advanced MIMO Rayleigh Distance

The nonlinear propagation phase, captured by the second-order Taylor expansion, introduces complex coupling components in MIMO configurations. Consequently, the LoS channel cannot always be modeled as a simple product of NF response vectors at the transmitter and receiver, as is done for NLoS channels, unless the UE lies beyond the advanced MIMO Rayleigh distance (MIMO-ARD) boundary [52]. Beyond this distance, coupling components can be safely neglected when modeling the LoS channel. This observation is critical, as it enables unified NLoS

frameworks for multipath channels even in the presence of a LoS path, thereby simplifying the overall channel representation.

3. NF Ray-Tracing Channel Models

This section presents the derived NF channel ray-tracing models for uniform linear and planar arrays (ULA, UPA). Detailed step-by-step derivations are provided in the Appendix, while the final expressions are summarized in Table 5. We then present the relation of these models to emerging 6G standardization efforts.

3.1. Model Formulation

In the multiple-input single-output (MISO) setup, the receiver is equipped with a single antenna while the transmitter employs either a ULA or UPA; conversely, the MIMO configuration assumes parallel-aligned arrays at both communication ends, enabling full exploitation of spatial multiplexing gains. For ULA-based systems, antenna elements are uniformly spaced along one dimension, while UPA configurations extend this arrangement to two dimensions on the xz-plane, with array response vectors separable along the x- and z-axes. The MIMO system layouts are depicted in Figure 3, while the MISO configuration can be visualized as a special case by simplifying the receiver to a single antenna, denoted by the subscript $\mathcal{T}$. The terms in Table 5 are described in Table 6, which employs cylindrical and spherical coordinates for 2D-ULA and 3D-UPA, respectively.

The LoS path represents a direct transmitter-receiver link characterized by spherical wavefront propagation without any obstacles blocking the path, and provides much higher signal strength compared to the reflected path. Whereas NLoS path captures reflected components via scatterers, modeled as cascaded LoS segments, i.e., from the transmitter to the scatterer, and from the scatterer to the receiver. Specifically, the scatterer can be viewed as a single-antenna relay, where the first segment forms a MISO channel and the second forms a SIMO channel.

Compared to the FF-MISO channel, the structural formulation remains similar across both array types. However, the key distinctions in NF modeling lie in the construction of its fundamental components: the complex gain matrix $\boldsymbol{\beta}_*$ and the array response vector $\mathbf{a}(\mathbf{r}_0, \mathbf{s}_0)$. The array response vector captures the relative phase differences across array elements with respect to a reference point. Under the spherical wavefront assumption, this vector inherently incorporates both angle and distance information, extending beyond the angle-only dependence of its FF counterpart. Meanwhile, the complex gain matrix accounts for three multiplicative factors governing channel power: free-space path loss following the conventional inverse-square law, effective aperture loss, and polarization loss. The latter two are governed by EM principles centered on angular alignment mismatch. In the FF, these differences remain nearly identical across all array elements; hence, they are normally omitted. However, as the distance decreases, these variations become increasingly pronounced.

The enhanced DoFs in NF-MIMO LoS channels arise from the coupling matrix $\mathbf{H}^c$ introduced by spherical wavefront propagation. In the FF region, this matrix reduces to an all-ones matrix, reflecting the planar wavefront intuition where all antenna pairs experience identical relative phase relationships. Consequently, the FF-LoS channel matrix is rank-one and able to decompose into a product of two independent vectors, which is similar to NLoS channel formulation. In contrast, spherical wavefront in NF region introduces a non-trivial coupling matrix $\mathbf{H}^c$ where each element depends jointly on both transmit and receive antenna indices, preventing factorization into separate transmit and receive components. Due to the rank deficiency of the FF channel via the directed path, MIMO can only enable spatial multiplexing by using multiple

Table 5. Summary of NF channel models for different configurations

Array	System	Path	Formula	Model
ULA	MISO	LoS	$\mathbf{H}^{\text{LoS}}_{\text{sR-ULA}} = \left[\boldsymbol{\beta}^{\mathcal{T}}_{*} \odot \mathbf{a}^{\mathcal{T}}_{\text{ULA}}(\mathbf{r}_0, \mathbf{s}_0)\right]^{\mathsf{T}}$	$\text{ULA}^{\text{LoS}}_{\text{MISO}}$
		NLoS	$\mathbf{H}^{\text{NLoS}}_{\text{sR-ULA}} = \sum_{l=1}^{L}\left[\boldsymbol{\beta}^{\mathcal{T}}_{*,l} \odot \mathbf{a}^{\mathcal{T}}_{\text{ULA}}(\hat{\mathbf{r}}_l, \mathbf{s}_0)\right]^{\mathsf{T}}$	$\text{ULA}^{\text{NLoS}}_{\text{MISO}}$
	MIMO	LoS	$\mathbf{H}^{\text{LoS}}_{\text{P-ULAs}} = \boldsymbol{\beta}_{*} \odot \left(\mathbf{a}^{\mathcal{R}}_{\text{ULA}}(\mathbf{r}_0, \mathbf{s}_0)\right)\left(\mathbf{a}^{\mathcal{T}}_{\text{ULA}}(\mathbf{r}_0, \mathbf{s}_0)\right)^{\mathsf{T}} \odot \mathbf{H}^{c}$	$\text{ULA}^{\text{LoS}}_{\text{MIMO}}$
		NLoS	$\mathbf{H}^{\text{NLoS}}_{\text{P-ULAs}} = \sum_{l=1}^{L}\boldsymbol{\beta}_{*,l} \odot \left(\mathbf{a}^{\mathcal{R}}_{\text{ULA}}(\mathbf{r}_0, \hat{\mathbf{r}}_l)\right)\left(\mathbf{a}^{\mathcal{T}}_{\text{ULA}}(\hat{\mathbf{r}}_l, \mathbf{s}_0)\right)^{\mathsf{T}}$	$\text{ULA}^{\text{NLoS}}_{\text{MIMO}}$
UPA	MISO	LoS	$\mathbf{H}^{\text{LoS}}_{\text{sR-UPA}} = \left[\boldsymbol{\beta}^{\mathcal{T}}_{*} \odot \mathbf{a}^{\mathcal{T}}_{\text{UPA}}(\mathbf{r}_{00}, \mathbf{s}_{00})\right]^{\mathsf{T}}$	$\text{UPA}^{\text{LoS}}_{\text{MISO}}$
		NLoS	$\mathbf{H}^{\text{NLoS}}_{\text{sR-UPA}} = \sum_{l=1}^{L}\left[\boldsymbol{\beta}^{\mathcal{T}}_{*,l} \odot \mathbf{a}^{\mathcal{T}}_{\text{UPA}}(\hat{\mathbf{r}}_l, \mathbf{s}_{00})\right]^{\mathsf{T}}$	$\text{UPA}^{\text{NLoS}}_{\text{MISO}}$
	MIMO	LoS	$\mathbf{H}^{\text{LoS}}_{\text{P-UPs}} = \boldsymbol{\beta}_{*} \odot \left(\mathbf{a}^{\mathcal{R}}_{\text{UPA}}(\mathbf{r}_{00}, \mathbf{s}_{00})\right)\left(\mathbf{a}^{\mathcal{T}}_{\text{UPA}}(\mathbf{r}_{00}, \mathbf{s}_{00})\right)^{\mathsf{T}} \odot \mathbf{H}^{c}$	$\text{UPA}^{\text{LoS}}_{\text{MIMO}}$
		NLoS	$\mathbf{H}^{\text{NLoS}}_{\text{P-UPAs}} = \sum_{l=1}^{L}\boldsymbol{\beta}_{*,l} \odot \left(\mathbf{a}^{\mathcal{R}}_{\text{UPA}}(\mathbf{r}_0, \hat{\mathbf{r}}_l)\right)\left(\mathbf{a}^{\mathcal{T}}_{\text{UPA}}(\hat{\mathbf{r}}_l, \mathbf{s}_0)\right)^{\mathsf{T}}$	$\text{UPA}^{\text{NLoS}}_{\text{MIMO}}$

Table 6. The descriptors of the channel model notations

Description	Expression
Number of scatterers	$L-1$
The index of NLoS path	$l = 1, \ldots, L$
Reference antenna of Tx-ULA	$\mathbf{s}_0 \cdot (0,0)$
Reference antenna of Rx-ULA	$\mathbf{r}_0 \cdot (r, \theta)$
l-th scatter in 2D space	$\hat{\mathbf{r}}_l \cdot (\hat{r}_l, \hat{\theta}_l)$
Reference antenna of Tx-UPA	$\mathbf{s}_{00} \cdot (0,0,0)$
Reference antenna of Rx-UPA	$\mathbf{r}_{00} \cdot (r, \theta, \phi)$
l-th scatter in 3D space	$\hat{\mathbf{r}}_l \cdot (\hat{r}_l, \hat{\theta}_l, \hat{\phi}_l)$
Complex gain matrices	$\boldsymbol{\beta}_{*}$
Near-field array response vector	$\mathbf{a}(\mathbf{r}_0, \mathbf{s}_0)$
Channel coupling components	$\mathbf{H}^{c}$

reflected paths realized through a rich scattering environment [33]. Hence, this coupling matrix is therefore not merely a mathematical component but its contribution of enhanced spatial DoF in LoS channel is essential for accurate capacity analysis and the multiplexing potential of 6G system within the realm of FC.

3.2. Relation to 6G Standards

The most recent standard for describing wireless channel models applicable to beyond-5G and 6G systems is 3GPP TR 38.901 version 19.2.0 (Release 19) [69]. This document establishes geometry-based stochastic models (GBSMs) for frequencies from 0.5 to 100 GHz. Crucially, this approach is fundamentally measurement-based. The underlying statistical distributions are rigorously extracted from extensive empirical channel sounding campaigns.

In the GBSM framework, the channel is represented as a superposition of multiple propagation paths. Each path is characterized by random variables whose empirical distributions depend on specific deployment scenarios, such as urban macrocell, urban microcell, suburban, and indoor environments. Key parameters include angles of departure (AoD), angles of arrival (AoA), path delays, shadowing, path loss, and cluster-wise power distributions. The stochastic modeling ensures that each realization of the channel is statistically consistent with the targeted propagation environment, while retaining a geometric interpretation through the spatial locations of Tx, Rx, and scatterers.

Mathematically, the NF-MIMO channel in 3GPP GBSM can be expressed at the element level. Specifically, let $\mathbf{H}_{m,n}$ denote the (m,n)-th entry of the MIMO channel matrix $\mathbf{H} \in \mathbb{C}^{N_R \times N_T}$, where $m \in \{1, \ldots, N_R\}$ and $n \in$

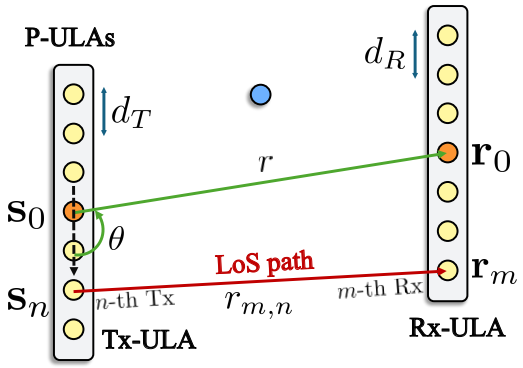

(a) Parallel ULAs system with LoS path

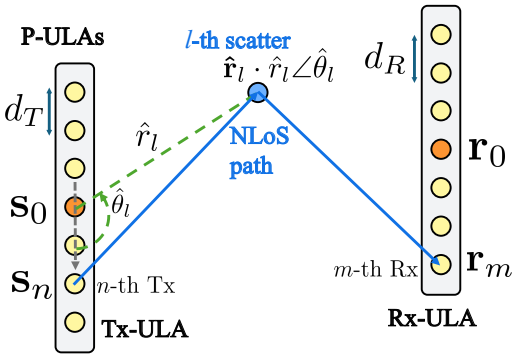

(b) Parallel ULAs system with NLoS path

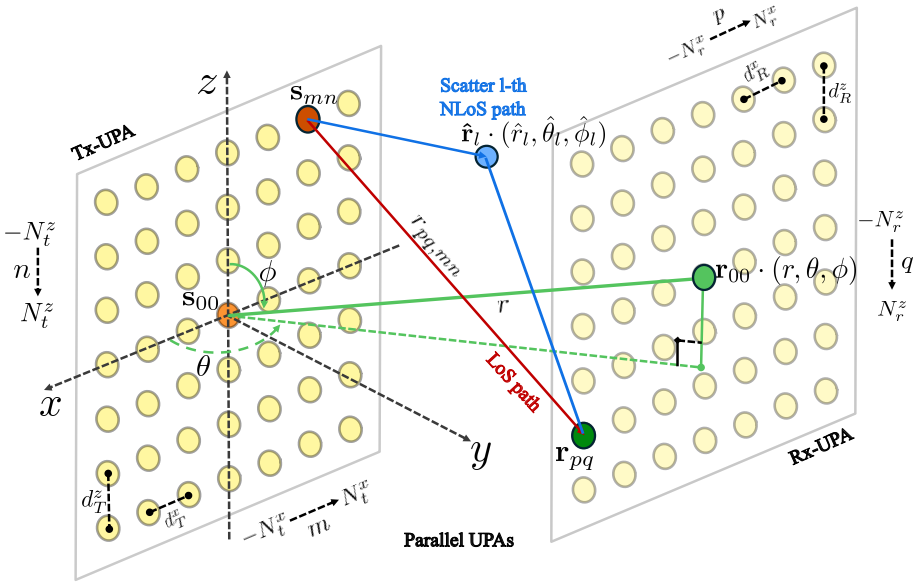

(c) Parallel UPAs system with LoS and NLoS paths

Figure 3. The layouts of the MIMO system.

$\{1, \ldots, N_T\}$ index the receive and transmit antenna elements, respectively (consistent with $\mathbf{a}^{\mathcal{R}}_{\text{ULA/UPA}}$ and $\mathbf{a}^{\mathcal{T}}_{\text{ULA/UPA}}$). According to 3GPP TR 38.901 [69], this entry is generated by summing over N_{cl} clusters, each comprising M_l sub-paths:

$$\mathbf{H}_{m,n} = \sum_{l=1}^{N_{\text{cl}}} \sum_{k=1}^{M_l} \sqrt{\frac{P_l}{M_l}} \mathbf{F}^{\mathsf{T}}_{\text{rx},m} \begin{bmatrix} e^{j\Phi^{vv}_{l,k}} & \sqrt{\kappa^{-1}}\, e^{j\Phi^{vh}_{l,k}} \\ \sqrt{\kappa^{-1}}\, e^{j\Phi^{hv}_{l,k}} & e^{j\Phi^{hh}_{l,k}} \end{bmatrix} \cdot \mathbf{F}_{\text{tx},n}\, e^{j\varphi^{(m,n)}_{l,k}}, \tag{3}$$

where P_l is the power of the l-th cluster (analogous to $|\boldsymbol{\beta}_{*,l}|^2$ in our model), $\mathbf{F}_{\text{rx},m}$ and $\mathbf{F}_{\text{tx},n}$ are the antenna field patterns at the m-th receive and n-th transmit elements, $\Phi^{(\cdot)}_{l,k} \in \{vv, vh, hv, hh\}$ are random initial phases for each polarization branch, where v and h denote vertical and horizontal polarizations, respectively, and κ is the cross-polarization power ratio (XPR). Table 7 summarizes the key similarities and differences between the ray-tracing channel models derived in this work and the 3GPP GBSM framework.

Table 7. Comparison between the NF ray-tracing models and 3GPP TR 38.901 GBSM

Aspect	**Presented Models**	**3GPP TR 38.901 GBSM**
Channel matrix assembly	$\mathbf{H}$ formed directly via outer product of $\mathbf{a}^{\mathcal{R}}$ and $\mathbf{a}^{\mathcal{T}}$, elementwise-weighted by $\boldsymbol{\beta}_*$ and $\mathbf{H}^c$	$\mathbf{H}_{m,n}$ assembled element-by-element from Eq. (3); no compact matrix factorization assumed
Path structure	LoS: single direct path; NLoS: L cascaded LoS segments via scatterers $\hat{\mathbf{r}}_l = (\hat{r}_l, \hat{\theta}_l)$	Unified cluster-subpath model; LoS added as deterministic component on top of N_{cl} stochastic clusters
Phase term	$\mathbf{a}_n^{\mathcal{T}} \cdot \mathbf{a}_m^{\mathcal{R}} \cdot \mathbf{H}_{m,n}^c$ derived from $\|\mathbf{r}_m - \hat{\mathbf{r}}_l\| + \|\hat{\mathbf{r}}_l - \mathbf{s}_n\|$	Identical two-hop distance $\|\mathbf{r}_m - \hat{\mathbf{r}}_{l,k}\| + \|\hat{\mathbf{r}}_{l,k} - \mathbf{s}_n\|$ per sub-path: **same physical principle**
Channel parameters	Deterministic: positions $\mathbf{r}_m, \mathbf{s}_n, \hat{\mathbf{r}}_l$ fully specified; $\boldsymbol{\beta}_*$ encodes path loss, aperture loss, polarization loss	Stochastic: $\hat{\mathbf{r}}_{l,k}$, AoD, AoA, P_l, shadow fading drawn from environment-specific distributions
Gain / polarization	Scalar mismatch factor in $\boldsymbol{\beta}_*$: $[\boldsymbol{\beta}_*]_{m,n} = \beta_{m,n}^{\text{PL}} \cdot \beta_{m,n}^{\text{aper}} \cdot \beta_{m,n}^{\text{pol}}$	Full 2×2 polarization matrix with XPR κ and random phases $\Phi^{vv/vh/hv/hh}$ per Eq. (3)
Spatial non-stationarity	$\boldsymbol{\beta}_*$ assumes uniform visibility across all elements	Partially modeled in Release 18/19 via visibility regions and cluster birth/death processes
Environment specificity	Geometry-driven only; no scenario tables	Urban macrocell, urban microcell, suburban, and indoor environments, etc. via standardized parameter tables

4. Channel Estimation

The previous section provided a summary of NF channel models for both MISO and MIMO (parallel-aligned) systems under ULA and UPA configurations. The transition to the NF regime not only increases computational burden due to spherical wavefront curvature but also introduces additional obstacles for accurate channel estimation. In this section, we present a systematic overview of existing NF channel estimation approaches, categorized into three main groups as shown in Table 8.

Compared to the baseline models derived earlier, the works reviewed here often incorporate additional features such as: spatial nonstationarity (SnS), hybrid-field propagation (HF), and multi-carrier usage (MC), which our framework can be readily extended to accommodate them. Specifically, SnS channels can be modeled by applying a binary mask to delineate visibility regions; hybrid-field scenarios typically arise from NLoS reflected paths where scatterers may be positioned in both NF and FF regions, and multi-carrier systems are employed to mitigate frequency selectivity in wideband communications.

4.1. Parametric Estimation-based Methods

Parametric estimator appears as an appealing approach for recovering the NF-LoS channel by estimating the UE position and substituting it into the channel model. A common choice for this approach is based on a two-stage multiple signal classification (MUSIC) approach [94], where the DoA of the UE can be firstly estimated, then the derivation of distance is obtained via conventional estimators, such as least-squares (LS) in [70], or minimum mean square error (MMSE) in [71]. The work in [72] further reduced complexity by decoupling these parameters for sequential estimation. Capturing the correlated feature on sequential pilot measurements, [73] exploited long short-term memory (LSTM) to

Table 8. Summary of NF channel estimation methods

Category	Ref.	System	Array	Path	Features	Algorithms	Model
Parametric Estimation-based Methods							
MUSIC method	[70]	MISO	UPA	LoS		LS-based two-stage	$\text{UPA}_{\text{MISO}}^{\text{LoS}}$
	[71]	MISO	UPA	LoS		MMSE-based two-stage	$\text{UPA}_{\text{MISO}}^{\text{LoS}}$
	[72]	MISO	UPA	LoS		Low-complexity SADCE	$\text{UPA}_{\text{MISO}}^{\text{LoS}}$
DL-based	[73]	MIMO	UPA	LoS		D-STiCE based on LSTM	$\text{UPA}_{\text{MISO}}^{\text{LoS}}$
Sparsity-Aware CS-based Methods							
Matching Pursuit	[51]	MISO	ULA	NLoS	MC	P-SOMP & P-SIGW	$\text{ULA}_{\text{MISO}}^{\text{NLoS}}$
	[55]	MISO	ULA	NLoS	SnS & MC	GP-SOMP & GP-SIGW	$\text{ULA}_{\text{MISO}}^{\text{NLoS}}$
	[74]	MISO	ULA	LoS	SnS	P-OMP & List-Type CE	$\text{ULA}_{\text{MISO}}^{\text{LoS}}$
	[52]	MIMO	ULA	Mixed		LoS & NLoS estimator	$\text{ULA}_{\text{MISO}}^{\text{Mixed}}$
Bayesian method	[75]	MISO	ULA	NLoS	MC	Adaptive JSBL-CE	$\text{ULA}_{\text{MISO}}^{\text{NLoS}}$
	[76]	MISO	ULA	NLoS	HF & MC	Hybrid-field JSBL	$\text{ULA}_{\text{MISO}}^{\text{NLoS}}$
	[77]	MISO	ULA	NLoS	HF	Augmented hybrid-field SBL	$\text{ULA}_{\text{MISO}}^{\text{NLoS}}$
	[78]	MISO	UPA	NLoS	SnS	MAP for joint VRs and CE	$\text{ULA}_{\text{MISO}}^{\text{NLoS}}$
Hybrid field	[53]	MISO	ULA	NLoS	HF	Dual-domain codebook	$\text{ULA}_{\text{MISO}}^{\text{NLoS}}$
	[79]	MISO	ULA	NLoS	HF	SGP-based two-stage	$\text{ULA}_{\text{MISO}}^{\text{NLoS}}$
	[61]	MIMO	ULA	Mixed	HF	Block-sparsity codebook	$\text{ULA}_{\text{MIMO}}^{\text{Mixed}}$
Beam splitting	[80]	MISO	ULA	NLoS	MC	Carrier-dependent codebook	$\text{ULA}_{\text{MISO}}^{\text{NLoS}}$
	[81]	MISO	ULA	NLoS	MC	BPD-based estimator	$\text{ULA}_{\text{MISO}}^{\text{NLoS}}$
2D & 3D codebook	[57]	MISO	ULA	NLoS	SnS	Scatter-wise & VR-wise	$\text{ULA}_{\text{MISO}}^{\text{NLoS}}$
	[82]	MISO	UPA	NLoS		TDP-decomposed sparisty	$\text{UPA}_{\text{MISO}}^{\text{NLoS}}$
Advanced codebook	[83]	MISO	ULA	LoS		DL-OMP	$\text{ULA}_{\text{MISO}}^{\text{NLoS}}$
	[84]	MIMO	ULA	Mixed		DPSS-based codebook	$\text{ULA}_{\text{MIMO}}^{\text{LoS}}$
Deep Learning-based Methods							
Deep Unfolding	[85]	MISO	ULA	NLoS		SDL-LISTA	$\text{ULA}_{\text{MISO}}^{\text{NLoS}}$
	[86]	MISO	ULA	NLoS		Sparse low-ADC unfodling	$\text{ULA}_{\text{MISO}}^{\text{NLoS}}$
	[87]	MISO	ULA	NLoS	MC	AMP-SBL unfolding	$\text{ULA}_{\text{MISO}}^{\text{NLoS}}$
	[88]	MISO	UPA	NLoS	SnS & MC	Unfolded PGD	$\text{UPA}_{\text{MISO}}^{\text{NLoS}}$
Denoising 2D-noisy channel	[89]	MISO	ULA	NLoS		Light-weight XLCNet	$\text{ULA}_{\text{MISO}}^{\text{NLoS}}$
	[54]	MISO	ULA	NLoS	HF	RACNN	$\text{ULA}_{\text{MISO}}^{\text{NLoS}}$
	[90]	MISO	UPA	NLoS	HF	FPN-OAMP	$\text{UPA}_{\text{MISO}}^{\text{NLoS}}$
	[91]	MISO	ULA	NLoS		P-MRDN estimator	$\text{ULA}_{\text{MISO}}^{\text{NLoS}}$
	[92]	MISO	ULA	NLoS	HF & MC	GDM-based estimator	$\text{ULA}_{\text{MISO}}^{\text{NLoS}}$
	[93]	MIMO	ULA	Mixed		GAN-based estimator	$\text{ULA}_{\text{MIMO}}^{\text{Mixed}}$

further improve estimation result with reduced pilot overhead. However, while parametric methods operating in continuous space achieve high accuracy, this method generally incurs significant computational cost [95].

4.2. Sparsity-Aware CS-based Methods

Exploiting the inherent sparsity of NF channels in the polar domain, combined with beam focusing, compressed sensing (CS) still remains an effective estimation scheme with reduced pilot overhead. However, the transition to the NF regime necessitates a fundamental redesign of the sparsifying dictionary, referred to as a codebook in this literature, and the intensive computation of baseband processing induced by spherical wavefront effects continues to hinder practical deployment of NFC for 6G systems [96]. Based on the type of sparsifying codebook employed, existing NF channel estimation works can be categorized as follows.

4.2.1. Coherence-based Polar Codebook

The polar-domain codebook introduced in [51], constructed by thresholding coherence values to establish a sparse representation for NF channels, has become a widely adopted choice for CS-based approaches. Building on this foundation, the authors proposed two-stage estimators realized through a codebook-based on-grid solution followed by an off-grid stage using maximum likelihood principle. Extending this work to address spatial nonstationarity, Chen *et al.* [55] introduced group time block coding (GTBC) to deal with scattering path variations, whereas Zhang *et al.* [74] focused on LoS path modeling, accommodating both known and unknown VR subarray partitions. For mixed propagation environments, Lu *et al.* [52] developed a unified framework accommodating both LoS and multipath models through MIMO-ARD measurements.

Building on sparse Bayesian learning (SBL), the adaptive JSBL-CE in [75] first obtained coarse angle estimates, then iteratively refines distances to improve accuracy without increasing codebook overhead. Extended to hybrid-field scenarios, Wang *et al.* [76] introduced Hybrid JSBL with a global sparse prior, while Djelouat *et al.* [77] augmented the SBL objective with two regularization terms. Parallel to these, Xu *et al.* [78] proposed a MAP framework with variational Bayesian inference (VBI) by three sub-modules: channel estimation, VR detection, and gradient-based grid update.

4.2.2. Application-tailored Codebooks

Recognizing that NF channels may exhibit sparsity across multiple domains, several works have developed hybrid codebook designs. Extended to the hybrid-field scenario combining NF and FF components, Wei *et al.* [53] proposed a dual-codebook combining DFT and polar-domain codebooks to exploit the sparsity characteristics of hybrid channels. Building on that foundation, Lei *et al.* [61] proposed two stochastic gradient pursuit (SGP)-based schemes employing a two-stage estimator. From another perspective, [79] proposed a block sparse representation of hybrid field channel based on a unitary matrix, which effectively mitigates coherence-related issues.

To mitigate the beam-split effect in NF-OFDM channels, subcarrier-dependent codebooks that explicitly account for both angular and distance deviations have been proposed in [80]. An alternative approach based on bilinear pattern detection (BPD) is introduced in [81] to accurately recover wideband XL-MIMO channels. This method is motivated by the observation that the NF beam-split effect exhibits a bilinear pattern, revealing a linear frequency-dependence in the sparse support sets of both the angle and distance domains.

4.2.3. Other Codebooks on Polar Domain

Addressing the nonstationary nature from both scatterer and subarray perspectives, Han *et al.* [57] proposed localizing scatterers and identifying their unique mapping to VRs, exploiting the resulting sparsity across the two-dimensional spatial domain. For UPA configurations, Guo *et al.* [82] focused on mitigating energy spread

by introducing triple-parameter decomposition (TPD), which handles azimuth angle, elevation angle, and distance in their own sparse domains, and presented an efficient scheme robust to cluster size and distance variations [97].

A fundamental challenge of conventional polar-domain codebooks is high coherence between columns, which degrades CS recovery performance. To address this bottleneck, Zhang *et al.* [83] proposed an alternative codebook that parameterizes distance through angular information, realized via a dictionary learning orthogonal matching pursuit (DL-OMP) algorithm for NF-LoS channel estimation. Exploiting eigenvalue decomposition (EVD), Liu *et al.* [84] introduced a discrete prolate spheroidal sequences (DPSS)-based codebook that overcomes the coherence bottleneck through inherent column-wise orthogonality, yielding significant codebook size reduction and enhanced computational efficiency over conventional polar designs.

4.3. Deep Learning-based Methods

To attain the goal of AI-native 6G, considerable research efforts have focused on embedding dynamic learning frameworks into complex signal processing tasks via model-based deep learning [98]. Compared to two approaches above, this learning-aided approach offers distinct advantages in computational efficiency and convergence rate, but requires an offline training stage.

4.3.1. Deep Unfolding-based Methods

A pivotal advancement in model-based deep learning came with the introduction of deep unfolding. Leveraging the iterative structure of the 'iterative shrinkage thresholding algorithm' (ISTA) [99], Gregor and LeCun [100] introduced this concept through learned ISTA (LISTA), a neural architecture that learns algorithm parameters from data to achieve fast sparse code approximations, with initial applications in image denoising and inpainting. Building upon this LISTA framework, Zhang *et al.* [85] proposed SDL-LISTA (sparsifying dictionary learning LISTA) for NF channel estimation, enhancing performance by formulating the sparsifying dictionary itself as a learnable neural layer embedded within the unfolded architecture.

The deep unfolding paradigm has since been extended to address specific challenges in 6G channel estimation. For systems employing low-resolution analog-to-digital converters to mitigate power consumption and hardware complexity, Ly *et al.* [86] developed an efficient on-grid estimator further refined through deep unfolding. To mitigate beam-split effects, Gao *et al.* [87] proposed a deep unfolding scheme that integrates learning dynamics with an iterative solution of sparse Bayesian learning (SBL). Extending this direction, Zheng *et al.* [88] introduced an unfolded projected gradient descent (PGD) method incorporating monotonic descent constraints across layers and a primal-dual training procedure for MAP-based channel estimation.

4.3.2. Denoising-based Methods

By reshaping channel representations as 2D matrices, convolutional neural networks have been leveraged to capture spatial features and effectively denoise channel images [101]. Building on this concept, Gao *et al.* [89] first obtain a coarse LS-based solution as a noisy image, and propose XLCNet for denoising, then further develop a lightweight version through weight pruning and quantization to reduce complexity and model size. Extending this direction, Lam *et al.* [54] introduce a residual attention convolutional neural network (RACNN) that enhances feature extraction during denoising, achieving improved performance for hybrid-field channel estimation.

Building on the fixed point network (FPN) framework, Yu *et al.* [90] proposed a contractive mapping architecture combining orthogonal approximate message passing (OAMP) with CNN-

based nonlinear estimators enhanced by residual connections. Meanwhile, Lei *et al.* [91] addressed the energy spread effect in polar-domain channel estimation through a multiple residual dense network (P-MRDN), building upon MRDN-based angular domain schemes [102].

Most recently, generative models have opened new frontiers for channel estimation. Jin *et al.* [92] proposed a generative diffusion model (GDM) conditioned on side information to refine coarse estimates from CS-based algorithms, while Ye *et al.* [93] employed an IE-Pix2pix framework with adversarial loss to govern training in a conditional generative adversarial network (CGAN) for enhanced estimation accuracy.

5. Challenges and Opportunities

5.1. Transition to NF Regime

Challenges: Accurately exhibiting the NF-EM characteristics of 6G systems presents significant modeling challenges due to the breakdown of traditional FF assumptions. The primary difficulty arises from the transition to a spherical wavefront model, where the EM phase is a nonlinear function of the antenna index, requiring the integration of both angle and propagation distance for precise characterization. This complexity is further exacerbated by spatial nonstationarity, a phenomenon where the massive aperture of ELAA results in different array segments perceiving unique VRs and experiencing non-uniform path losses.

Opportunities: NFC transforms the 6G landscape by evolving traditional space division multiple access (SDMA) into LDMA. By exploiting the distance domain, LDMA utilizes precise beamfocusing to serve multiple users at the same angle but varying ranges, a capability further enhanced by NOMA for massive connectivity [23]. Beyond access schemes, the spherical wavefront curvature offers enhanced DoFs in the rank of LoS MIMO channels, enabling high-rate spatial multiplexing even in scattering-sparse environments [103]. Furthermore, the distance-dependent phase encoding allows for centimeter-level localization and sensing from single anchor nodes, while the spatial selectivity of focused energy provides a robust layer of physical layer security against eavesdropping [104]. To validate the practical feasibility of these potentials, recent studies have introduced early hardware testbeds. For instance, scalable prototypes for mid-band XL-MIMO systems have been developed to evaluate practical NF performance [105]. Furthermore, extensive channel sounding campaigns using ELAA prototypes have physically captured NF propagation characteristics [106], while other experimental setups have successfully validated NF beamfocusing capabilities in real-world scenarios [107].

5.2. Computational Complexity

Challenges: High dimensionality measurements of ELAs render traditional estimation techniques impractical due to excessive pilot overhead [60]. Transitioning from 1D angular to 2D polar-domain processing drastically increases codebook size and baseband computational load [51]. This complexity extends to 3D beam training, requiring highly efficient protocols to navigate the expanded search space [15, 32]. Furthermore, spatial nonstationarity and beam-split effects demand complicated frequency-dependent algorithms to compensate for severe array gain loss [26].

Opportunities: Overcoming these issues demands advanced architectural and algorithmic solutions. The AoSA architecture mitigates this burden through subarray-level processing, reducing circuit devices and simplifying baseband-to-RF operations [14]. More radically, stacked intelligent metasurfaces (SIM) enable wave-domain precoding and combining; signal propagation through physical layers at the speed of light dramatically reduces both latency and digital base-band complexity [108]. Model-based

deep learning, such as deep unfolding, addresses the huge computational burden of NF XL-MIMO processing by embedding domain knowledge of unique EM traits directly into a theoretical optimizer with the aid of learning framework [98]. This approach may achieve high-accuracy estimation with significantly lower training overhead and pilot requirements than conventional data-driven methods.

5.3. CAP-MIMO Antennas and EIT

Challenges: CAP-MIMO antennas, also referred to as holographic MIMO, will eventually push traditional communication models to their limits through near-continuous surfaces. This transition replaces tractable matrix operations with complex integral calculations, creating prohibitive computational burdens for real-time processing [109, 110]. Conventional channel estimation methods fail because discrete measurements are incompatible with continuous apertures [111]. Furthermore, extreme antenna density introduces mutual coupling, thermal noise, and radiation inefficiency [15, 32]. Finally, EIT is still in its early stages; translating its complex physics into practical, low-complexity hardware designs remains a major problem, especially when accounting for power saturation in large surfaces [112].

Opportunities: Despite their own challenges, CAP-MIMO and EIT form a perfect duality. CAP-MIMO will offer nearly infinite spatial degrees of freedom through optimized current distributions and enable extreme spatial multiplexing and depth-domain exploitation via schemes like LDMA [26, 33]. This is when EIT becomes apparent, since it provides a consistent framework grounded in Maxwell's equations. It replaces discrete matrix models with bounded linear operators by Green's functions, which accurately capture NF spherical wavefronts, tri-polarization, and evanescent waves phenomena that the FF assumption omitted [36]. Together, they bridge the gap between physics and communication, leading to future networks that are simultaneously physically consistent and tractable [112].

5.4. Localization and Sensing

Challenges: ISAC has been pointed out as one of the key usage scenarios of the 6G cellular network [5, 113]. As most existing localization algorithms were developed for the FF model, achieving the targeted sub-10 cm localization accuracy in the NF remains challenging. The spherical wave property increases the model complexity and necessitates the study of efficient localization algorithms, especially when low latency is required [114]. The popular deployment of hybrid beamforming transceivers amplifies the coupling effect between VRs and the beam-split effect [115], making the sensing task more difficult as the sparsity structure is damaged. User mobility creates additional difficulty for NF-ISAC systems, since high-speed targets induce non-uniform Doppler shifts across ELAAs and invalidate conventional FFT-based velocity estimation. This effect produces highly coupled signal structures that are naturally represented by complex high-order tensors spanning spatial, temporal, and frequency dimensions [116].

Opportunities: Fortunately, the NF characteristics also provide several opportunities to enhance sensing accuracy. The spherical wave propagation and beamfocusing capability enable high-resolution localization in both the angle and range domains. In addition, spatial nonstationarity across ELAAs allows passive sensing through channel blockages and channel variations [114]. By properly controlling the focal points induced by the beam-split effect, the system can achieve accurate user localization with reduced training overhead [58]. A cross-shaped antenna architecture can further exploit these properties. This architecture is a planar antenna configuration composed of two orthogonal linear arrays (LAs) intersecting at their centers,

forming a cross-shaped structure [117, 118]. This geometry enables the decoupled estimation of spatial parameters along the two array branches and therefore reduces the computational complexity of localization algorithms [119–121], especially when co-prime LAs are used. The UCA structure also provides additional spatial degrees of freedom and facilitates automatic parameter pairing during the localization process.

6. Conclusions

This article has established a comprehensive overview of near-field communications for 6G systems, with three main thrusts. We began by examining the fundamental electromagnetic properties induced by ELAA and THz deployment and clarified the distance boundaries that partition the radiating space into distinct regions with unique phase and amplitude characteristics. Building on this foundation, we have presented an overview of ray-tracing channel models for both uniform linear and planar arrays.

We have contrasted the presented deterministic ray-tracing models with the standardized framework by highlighting the key similarities and differences between them. We have also provided a systematic review of existing near-field channel estimation techniques, categorized into parametric, sparsity-aware CS-based, and deep learning-based methods.

Finally, we have identified critical challenges and emerging opportunities, such as: NF transition, computational complexity, CAP-MIMO and EIT integration, and localization and sensing, which align future research and underscore the prospects of NF propagation in the 6G paradigm.

Acknowledgment

This research was funded by the research project QG.25.08 of Vietnam National University, Hanoi.

Appendix A.1 NF Ray-Tracing Channel

This section presents rigorous site-specific near-field channel models for uniform linear and planar arrays (ULA, UPA). Our work also provides a comprehensive mathematical derivation of distinctive propagation regions, establishing a robust theoretical foundation for evaluating unique near-field electromagnetic characteristics and analyzing the accurate potentials of NFC for 6G systems.

A.1.1 ULA - Uniform Linear Array

A ULA consists of antenna elements arranged linearly with equal spacing. This subsection considers a MIMO system where both the transmitter (Tx) and receiver (Rx) employ ULAs, as illustrated in Fig. 4. The key system parameters and coordinates are summarized in Table 9.

Let $L-1$ denote the total number of scatterers in the environment, with $\hat{\mathbf{r}}_l$ representing the coordinate of the l-th scatterer. The receiver captures signals via two mechanisms: a direct line-of-sight (LoS) path from the transmitter and reflected non-line-of-sight (NLoS) paths from scatterers. The overall channel matrix can thus

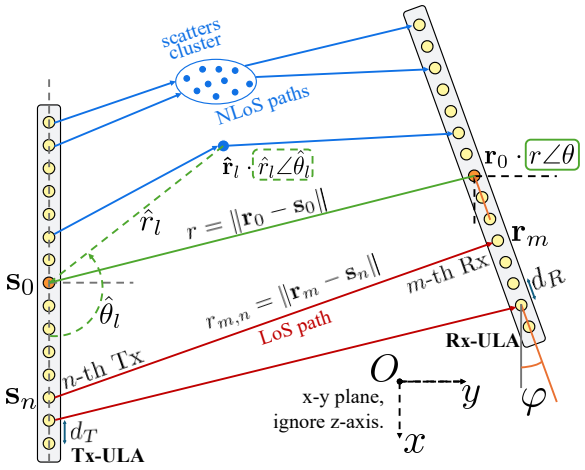

Figure 4. The general assumption for ULAs system employed at both Tx and Rx sides.

Table 9. System parameters and coordinates of Tx & Rx ULA antenna elements.

Description	Expression
Number of Tx antennas.	$N_{\mathcal{T}} = 2N_t + 1$
Tx antenna index	$n \in \{-N_t, \cdots, N_t\}$
Tx antenna spacing	d_T
Number of Rx anten.	$N_{\mathcal{R}} = 2N_r + 1$
Rx antenna index	$m \in \{-N_r, \cdots, N_r\}$
Rx antenna spacing	d_R
Number of scatterers	$L - 1$
Center of Tx array	$\mathbf{s}_0 = (0, 0)$
Center of Rx array	$\mathbf{r}_0 = (r\cos\theta,\ r\sin\theta)$
Relative angle	φ
n-th Tx element	$\mathbf{s}_n = (nd_T,\ 0)$
m-th Rx element	$\mathbf{r}_m = \begin{pmatrix} r\cos\theta - md_R\cos\varphi, \\ r\sin\theta - md_R\sin\varphi \end{pmatrix}$
Reference distance	$r = \|\mathbf{r}_0 - \mathbf{s}_0\|$
Distance Tx – Rx	$r_{m,n} = \|\mathbf{r}_m - \mathbf{s}_n\|$

be expressed as

$$\mathbf{H}_{\text{ULA}}(\mathbf{r}_0, \mathbf{s}_0) \in \mathbb{C}^{N_{\mathcal{R}} \times N_{\mathcal{T}}} = \mathbf{H}_{\text{ULA}}^{\text{LoS}}(\mathbf{r}_0, \mathbf{s}_0) + \sum_{l=1}^{L} \mathbf{H}_{\text{ULA}}^{\text{NLoS}}(\mathbf{r}_0, \mathbf{s}_0, \hat{\mathbf{r}}_l), \tag{A.1.1}$$

where $\mathbf{H}_{\text{ULA}}^{\text{LoS}}$ represents the LoS component and $\mathbf{H}_{\text{ULA}}^{\text{NLoS}}$ represents the contribution from the l-th scatterer. For the LoS path, the channel coefficient of the propagation link between the n-th element of Tx and m-th element of Rx is given by $h_{m,n}$, then the overall LoS channel connecting all antenna elements together can be formulated by $\mathbf{H}_{\text{ULA}}^{\text{LoS}}$, whose (m, n)-th entry is assigned by

$$h_{m,n} := h(\mathbf{r}_m, \mathbf{s}_n) = \beta_{m,n} \exp\left(-j\tfrac{2\pi}{\lambda} r_{m,n}\right) = \beta_{m,n} \exp\left(-j\tfrac{2\pi}{\lambda} r\right) \exp\left(-j\phi_{m,n}\right), \tag{A.1.2}$$

where the channel amplitude and propagation phase for that link can be denoted as $\beta_{m,n}$ and $\phi_{m,n}$, respectively, with

$$\phi_{m,n} = \tfrac{2\pi}{\lambda}\,(r_{m,n} - r), \tag{A.1.3a}$$

$$r_{m,n} = \|\mathbf{r}_m - \mathbf{s}_n\| = \sqrt{\begin{matrix}(r\cos\theta - md_R\cos\varphi - nd_T)^2 \\ +(r\sin\theta - md_R\sin\varphi)^2.\end{matrix}} \tag{A.1.3b}$$

The amplitude gain $\beta_{m,n}$ in Eq. (A.1.2) may be treated as uniform across all antenna pairs in the UPW and USW regions, but varies significantly in the NUSW region. Detailed closed-form expressions for different regions will be derived in subsequent sections.

Each NLoS path involves reflection from a scatterer and can be modeled as a cascade of two LoS segments, i.e., from the transmitter to the scatterer, and from the scatterer to the receiver. Specifically, the scatterer acts as a single-antenna relay, where the first segment forms a MISO channel and the second forms a SIMO channel. The channel coefficient for the l-th scatterer path between the n-th Tx element and the m-th Rx element is given by

$$\left[\mathbf{H}_{\text{ULA}}^{\text{NLoS}}(\mathbf{r}_0, \mathbf{s}_0, \hat{\mathbf{r}}_l)\right]_{m,n} = h(\mathbf{r}_m, \hat{\mathbf{r}}_l) \cdot h(\hat{\mathbf{r}}_l, \mathbf{s}_n). \tag{A.1.4}$$

A.1.1.1 Parallel ULAs - LoS channel

For simplicity to facilitate analysis, we consider a parallel ULA (P-ULA) configuration where the transmit and receive arrays are perfectly aligned, i.e., $\varphi = 0$, as depicted in Fig. 5. Under this assumption, the distance simplifies to

$$r_{m,n} = \sqrt{\begin{matrix}r^2 + (nd_T + md_R)^2 \\ -2r\cos\theta(md_R + nd_T)\end{matrix}}. \tag{A.1.5}$$

Applying a second-order Taylor expansion $\sqrt{1+x} \approx 1 + x/2 - x^2/8$ yields

$$r_{m,n} \approx r + \left(\tfrac{nd_T \cdot md_R \sin^2\theta}{r}\right) + \left(-nd_T\cos\theta + \tfrac{n^2 d_T^2 \sin^2\theta}{2r}\right) + \left(-md_R\cos\theta + \tfrac{m^2 d_R^2 \sin^2\theta}{2r}\right). \tag{A.1.6}$$

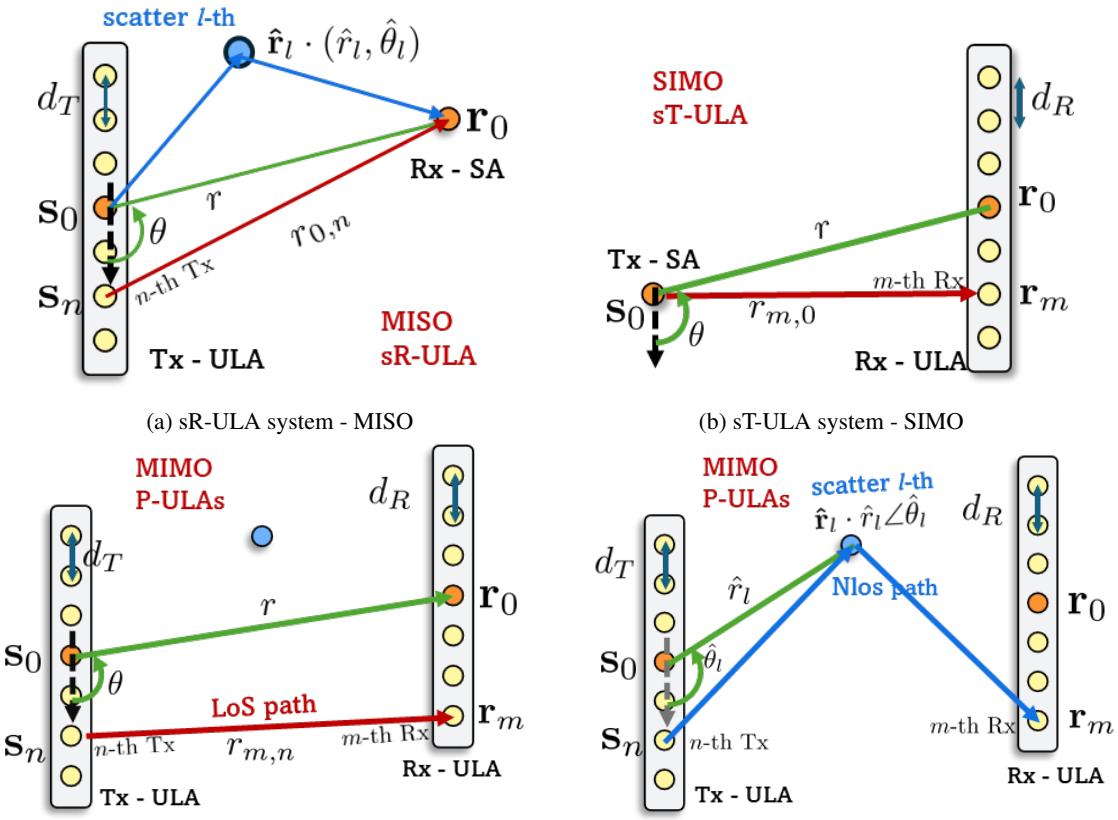

(a) sR-ULA system - MISO

(b) sT-ULA system - SIMO

(c) Parallel ULAs system - LoS path

(d) Parallel ULAs system - NLoS path

Figure 5. The Parallel ULAs system and the single-antenna & ULA configurations.

This approximation allows us to decompose the expression into three terms; the first one jointly depends on both m and n, referred to as the coupling component, while the two remaining terms depend only on either n or m corresponding to antenna index of either Tx and Rx system, respectively. The propagation phase $\phi_{m,n} = \frac{2\pi}{\lambda}(r_{m,n} - r)$ can therefore be decomposed as

$$\begin{aligned}\phi_{m,n} &= \tfrac{2\pi}{\lambda}\,(r_{m,n} - r) \\ &= \phi^c_{m,n} + \phi_{0,n} + \phi_{m,0}, \end{aligned} \tag{A.1.7}$$

where the derivation of each term can be given by

$$\phi^c_{m,n} = \tfrac{2\pi}{\lambda}\left(\tfrac{nd_T \cdot md_R \sin^2\theta}{r}\right), \tag{A.1.8a}$$

$$\phi_{0,n} = \tfrac{2\pi}{\lambda}\left(-nd_T\cos\theta + \tfrac{n^2 d_T^2 \sin^2\theta}{2r}\right), \tag{A.1.8b}$$

$$\phi_{m,0} = \tfrac{2\pi}{\lambda}\left(-md_R\cos\theta + \tfrac{m^2 d_R^2 \sin^2\theta}{2r}\right). \tag{A.1.8c}$$

Using the phase decomposition above, the LoS channel coefficient between the n-th Tx antenna and m-th Rx antenna can be expressed as

$$\begin{aligned} h(\mathbf{r}_m, \mathbf{s}_n) &= \left[\mathbf{H}^{\text{LoS}}_{\text{P-ULAs}}\right]_{m,n} \\ &= \beta_{m,n}\exp\left(-j\tfrac{2\pi}{\lambda}r\right)\exp(-j\cdot\phi_{m,n}) \\ &= \beta^*_{m,n}\cdot a^{\mathcal{R}}_{\text{ULA}}(\mathbf{r}_m, \mathbf{s}_0)\cdot a^{\mathcal{T}}_{\text{ULA}}(\mathbf{r}_0, \mathbf{s}_n)\cdot h^c_{m,n}, \end{aligned} \tag{A.1.9}$$

where each term is defined as in the following.

The complex channel gain $\boldsymbol{\beta}_* \in \mathbb{C}^{N_{\mathcal{R}}\times N_{\mathcal{T}}}$:

$$\beta^*_{m,n} = [\boldsymbol{\beta}_*]_{m,n} = \beta_{m,n}\exp\left(-j\tfrac{2\pi}{\lambda}r\right). \tag{A.1.10}$$

incorporating both the amplitude and the center-to-center phase shift.

The Tx array response vector $\mathbf{a}^{\mathcal{T}}_{\text{ULA}} \in \mathbb{C}^{N_{\mathcal{T}}\times 1}$: The n-th element captures the phase contribution

dependent only on the Tx antenna index:

$$a^{\mathcal{T}}_{\text{ULA}}(\mathbf{r}_0, \mathbf{s}_n) = \left[\mathbf{a}^{\mathcal{T}}_{\text{ULA}}(\mathbf{r}_0, \mathbf{s}_0)\right]_n = \exp(-j\,\phi_{0,n}) \tag{A.1.11}$$

Rx array response vector $\mathbf{a}^{\mathcal{R}}_{\text{ULA}} \in \mathbb{C}^{N_{\mathcal{R}}\times 1}$: The m-th element captures the phase contribution dependent only on the Rx antenna index:

$$a^{\mathcal{R}}_{\text{ULA}}(\mathbf{r}_m, \mathbf{s}_0) = \left[\mathbf{a}^{\mathcal{R}}_{\text{ULA}}(\mathbf{r}_0, \mathbf{s}_0)\right]_m = \exp(-j\,\phi_{m,0}) \tag{A.1.12}$$

Coupling component $\mathbf{H}^c \in \mathbb{C}^{N_{\mathcal{R}}\times N_{\mathcal{T}}}$ captures the joint dependence on both array indices.

$$h^c_{m,n} = [\mathbf{H}^c]_{m,n} = \exp\left(-j\phi^c_{m,n}\right) \tag{A.1.13}$$

Collecting all antenna pairs, the LoS channel matrix for parallel ULAs can be written in compact form as

The LoS channel of P-ULAs system

$$\mathbf{H}^{\text{LoS}}_{\text{P-ULAs}}(\mathbf{r}_0, \mathbf{s}_0) \in \mathbb{C}^{N_{\mathcal{R}}\times N_{\mathcal{T}}} = \boldsymbol{\beta}_* \odot \left(\mathbf{a}^{\mathcal{R}}_{\text{ULA}}(\mathbf{r}_0, \mathbf{s}_0)\right)\left(\mathbf{a}^{\mathcal{T}}_{\text{ULA}}(\mathbf{r}_0, \mathbf{s}_0)\right)^{\mathsf{T}} \odot \mathbf{H}^c. \tag{A.1.14}$$

The array response vectors at Tx and Rx side is denoted by $\mathbf{a}^{\mathcal{T}}_{\text{ULA}}$ and $\mathbf{a}^{\mathcal{R}}_{\text{ULA}}$, respectively; they describe the relative phase shift experienced by each antenna element in the array due to the physical separation between them and their reference antenna indexed by $\mathbf{r}_o$ or $\mathbf{s}_o$. The coupling matrix $\mathbf{H}^c$ captures the interaction between Tx and Rx antenna pairs that cannot be separated into a product of individual array responses. This coupling is responsible for the increased spatial degrees of freedom (DoF) in near-field LoS MIMO channels compared to their far-field rank-one counterparts. When the communication distance exceeds the MIMO-ARD, the coupling phase $\phi^c_{m,n}$ becomes negligible, and $h^c_{m,n}$ approaches to unity, allowing the channel to be approximated by a rank-one structure [52].

A.1.1.2 Single-antenna and ULA - LoS channel

We first consider a MISO configuration where the receiver is equipped with a single antenna ($N_{\mathcal{R}} = 1$, i.e., $m = 0$), while the transmitter maintains a ULA. Using the phase decomposition in Eq. (A.1.7) with $m = 0$, the LoS channel coefficient between the n-th Tx element and the single Rx antenna simplifies to

$$\begin{aligned} h(\mathbf{r}_0, \mathbf{s}_n) &= \beta_{0,n} \exp\left(-j\tfrac{2\pi}{\lambda} r\right) \exp\left(-j \cdot \phi_{0,n}\right) \\ &= \beta^*_{0,n} \cdot a^{\mathcal{T}}_{\text{ULA}}(\mathbf{r}_0, \mathbf{s}_n), \end{aligned} \tag{A.1.15}$$

where $\beta^*_{0,n}$ is the corresponding complex channel gain to $\beta_{0,n}$. Collecting all Tx antenna elements, the overall complex gain vector at the transmitter $\boldsymbol{\beta}^{\mathcal{T}}_*$ can be computed as

$$\begin{aligned} \boldsymbol{\beta}^{\mathcal{T}}_* &= \left[\,\cdots,\, \beta^*_{0,n},\, \cdots\,\right]^{\mathsf{T}} \in \mathbb{C}^{N_{\mathcal{T}}\times 1}, \\ \beta^*_{0,n} &= \beta_{0,n} \exp\left(-j\tfrac{2\pi}{\lambda} r\right). \end{aligned} \tag{A.1.16}$$

The LoS channel of sR-ULA

$$\left[\mathbf{H}^{\text{LoS}}_{\text{sR-ULA}}\right]_{0,n} = h(\mathbf{r}_0, \mathbf{s}_n) \tag{A.1.17}$$

$$\begin{aligned} \mathbf{H}^{\text{LoS}}_{\text{sR-ULA}} &= \mathbf{h}^{\mathcal{T}}_{\text{ULA}}(\mathbf{r}_0, \mathbf{s}_0) \in \mathbb{C}^{1\times N_{\mathcal{T}}}, \\ &= \left[\boldsymbol{\beta}^{\mathcal{T}}_* \odot \mathbf{a}^{\mathcal{T}}_{\text{ULA}}(\mathbf{r}_0, \mathbf{s}_0)\right]^{\mathsf{T}}. \end{aligned} \tag{A.1.18}$$

Conversely, for a SIMO configuration where the transmitter has a single antenna ($N_{\mathcal{T}} = 1$, i.e., $n = 0$) and the receiver employs a ULA, the complex gain vector at the receiver is

$$\begin{aligned} \boldsymbol{\beta}^{\mathcal{R}}_* &= \left[\,\cdots,\, \beta^*_{m,0},\, \cdots\,\right]^{\mathsf{T}} \in \mathbb{C}^{N_{\mathcal{R}}\times 1}, \\ \beta^*_{m,0} &= \beta_{m,0} \exp\left(-j\tfrac{2\pi}{\lambda} r\right). \end{aligned} \tag{A.1.19}$$

The LoS channel coefficient between the single Tx antenna and the m-th Rx element becomes

$$\begin{aligned} \left[\mathbf{H}^{\text{LoS}}_{\text{sT-ULA}}\right]_{m,0} &= h(\mathbf{r}_m, \mathbf{s}_0) = h_{m,0} \\ &= \beta^*_{m,0} \cdot a^{\mathcal{R}}_{\text{ULA}}(\mathbf{r}_m, \mathbf{s}_0). \end{aligned} \tag{A.1.20}$$

The LoS channel of sT-ULA

$$\begin{aligned}\mathbf{H}_{\text{sT-ULA}}^{\text{LoS}} &= \mathbf{h}_{\text{ULA}}^{\mathcal{R}}(\mathbf{r}_0, \mathbf{s}_0) \in \mathbb{C}^{N_{\mathcal{R}}\times 1},\\ &= \boldsymbol{\beta}_*^{\mathcal{R}} \odot \mathbf{a}_{\text{ULA}}^{\mathcal{R}}(\mathbf{r}_0, \mathbf{s}_0). \end{aligned} \tag{A.1.21}$$

A.1.1.3 ULA - Multi-path channels

Consider an environment with $L-1$ scatterers, each contributes to an NLoS path from transmitter to receiver via reflection. The l-th NLoS path can be modeled as a cascade of two LoS segments: transmitter-to-scatterer and scatterer-to-receiver. Following the structure established for single-antenna configurations, the NLoS channel matrix for the l-th scatterer is

The NLoS channel of P-ULAs system

$$\begin{aligned}\mathbf{H}_{\text{P-ULAs}}^{\text{NLoS}}(\mathbf{r}_0, \mathbf{s}_0, \hat{\mathbf{r}}_l) &= \mathbf{h}_{\text{ULA}}^{\mathcal{R}}(\mathbf{r}_0, \hat{\mathbf{r}}_l)\, \mathbf{h}_{\text{ULA}}^{\mathcal{T}}(\hat{\mathbf{r}}_l, \mathbf{s}_0)\\ &= \left[\boldsymbol{\beta}_{*,l}^{\mathcal{R}} \odot \mathbf{a}_{\text{ULA}}^{\mathcal{R}}(\mathbf{r}_0, \hat{\mathbf{r}}_l)\right]\left[\boldsymbol{\beta}_{*,l}^{\mathcal{T}} \odot \mathbf{a}_{\text{ULA}}^{\mathcal{T}}(\hat{\mathbf{r}}_l, \mathbf{s}_0)\right]^{\mathsf{T}}\\ &= \boldsymbol{\beta}_{*,l} \odot \left(\mathbf{a}_{\text{ULA}}^{\mathcal{R}}(\mathbf{r}_0, \hat{\mathbf{r}}_l)\right)\left(\mathbf{a}_{\text{ULA}}^{\mathcal{T}}(\hat{\mathbf{r}}_l, \mathbf{s}_0)\right)^{\mathsf{T}}, \end{aligned} \tag{A.1.22}$$

where $\boldsymbol{\beta}_{*,l} = \left[\boldsymbol{\beta}_{*,l}^{\mathcal{R}}\right]\left[\boldsymbol{\beta}_{*,l}^{\mathcal{T}}\right]^{\mathsf{T}} \in \mathbb{C}^{N_{\mathcal{R}}\times N_{\mathcal{T}}}$ denotes the joint complex gain matrix for the l-th path. The individual terms follow the same construction as in Eq. (A.1.16) and Eq. (A.1.19), with distances computed relative to the scatterer position $\hat{\mathbf{r}}_l$.

Considering a MISO configuration where the receiver is equipped with a single antenna, the NLoS channel matrix computed for the l-th scatterer is

The NLoS channel of sR-ULA system

$$\mathbf{H}_{\text{sR-ULA}}^{\text{NLoS}} = \sum_{l=1}^{L}\left[\boldsymbol{\beta}_{*,l}^{\mathcal{T}} \odot \mathbf{a}_{\text{ULA}}^{\mathcal{T}}(\hat{\mathbf{r}}_l, \mathbf{s}_0)\right]^{\mathsf{T}} \tag{A.1.23}$$

A.1.2 UPA - Uniform Plane Array

A UPA extends the ULA concept to two dimensions, with antenna elements arranged in a rectangular grid on the xz-plane. For simplicity, we consider parallel UPAs (P-UPAs) where the receive array is oriented parallel to the transmit array. The system geometry is illustrated in Fig. 6, with key parameters summarized in Table 10.

A.1.2.1 Parallel UPA - LoS channel

Following the same approach as for ULAs, the channel coefficient between the (m,n)-th Tx element and the (p,q)-th Rx element is

$$\begin{aligned} h(\mathbf{r}_{pq}, \mathbf{s}_{mn}) &= \beta_{pq,mn}\exp\left(-j\tfrac{2\pi}{\lambda}r_{pq,mn}\right)\\ &= \beta_{pq,mn}\exp\left(-j\tfrac{2\pi}{\lambda}r\right)\exp\left(-j\cdot\phi_{pq,mn}\right)\\ &= \beta_{pq,mn}^{*}\exp(-j\cdot\phi_{pq,mn}), \end{aligned} \tag{A.1.24}$$

where the propagation phase $\phi_{pq,mn}$ can be decomposed into separable components as:

$$\begin{aligned}\phi_{pq,mn} &= \tfrac{2\pi}{\lambda}(r_{pq,mn} - r)\\ &= \phi_{00,mn} + \phi_{pq,00} + \phi_{p,m}^{cx} + \phi_{q,n}^{cz}, \end{aligned} \tag{A.1.25a}$$

$$\phi_{00,mn} = \phi_{00,m0} + \phi_{00,0n}, \tag{A.1.25b}$$

$$\phi_{pq,00} = \phi_{p0,00} + \phi_{0q,00}. \tag{A.1.25c}$$

For the ease of notation, we define γ as $\cos\gamma = \cos\theta\sin\phi$, then $\sin^2\gamma = 1 - \cos^2\theta\sin^2\phi$. The definitions of those phases are obtained as:

$$\phi_{00,m0} = \tfrac{2\pi}{\lambda}\left(-md_T^x\cos\gamma + \tfrac{(md_T^x)^2 sin^2\gamma}{2r}\right) \tag{A.1.26a}$$

$$\phi_{00,0n} = \tfrac{2\pi}{\lambda}\left(-nd_T^z\cos\phi + \tfrac{(nd_T^z)^2\sin^2\phi}{2r}\right) \tag{A.1.26b}$$

$$\phi_{p0,00} = \tfrac{2\pi}{\lambda}\left(-pd_R^x\cos\gamma + \tfrac{(pd_R^x)^2\sin^2\gamma}{2r}\right) \tag{A.1.26c}$$

$$\phi_{0q,00} = \tfrac{2\pi}{\lambda}\left(-qd_R^z\cos\phi + \tfrac{(qd_R^z)^2\sin^2\phi}{2r}\right) \tag{A.1.26d}$$

$$\phi_{p,m}^{cx} = \tfrac{2\pi}{\lambda}\tfrac{md_T^x pd_R^x\sin^2\gamma}{2r} \tag{A.1.26e}$$

$$\phi_{q,n}^{cz} = \tfrac{2\pi}{\lambda}\tfrac{nd_T^z qd_R^z\sin^2\phi}{2r} \tag{A.1.26f}$$

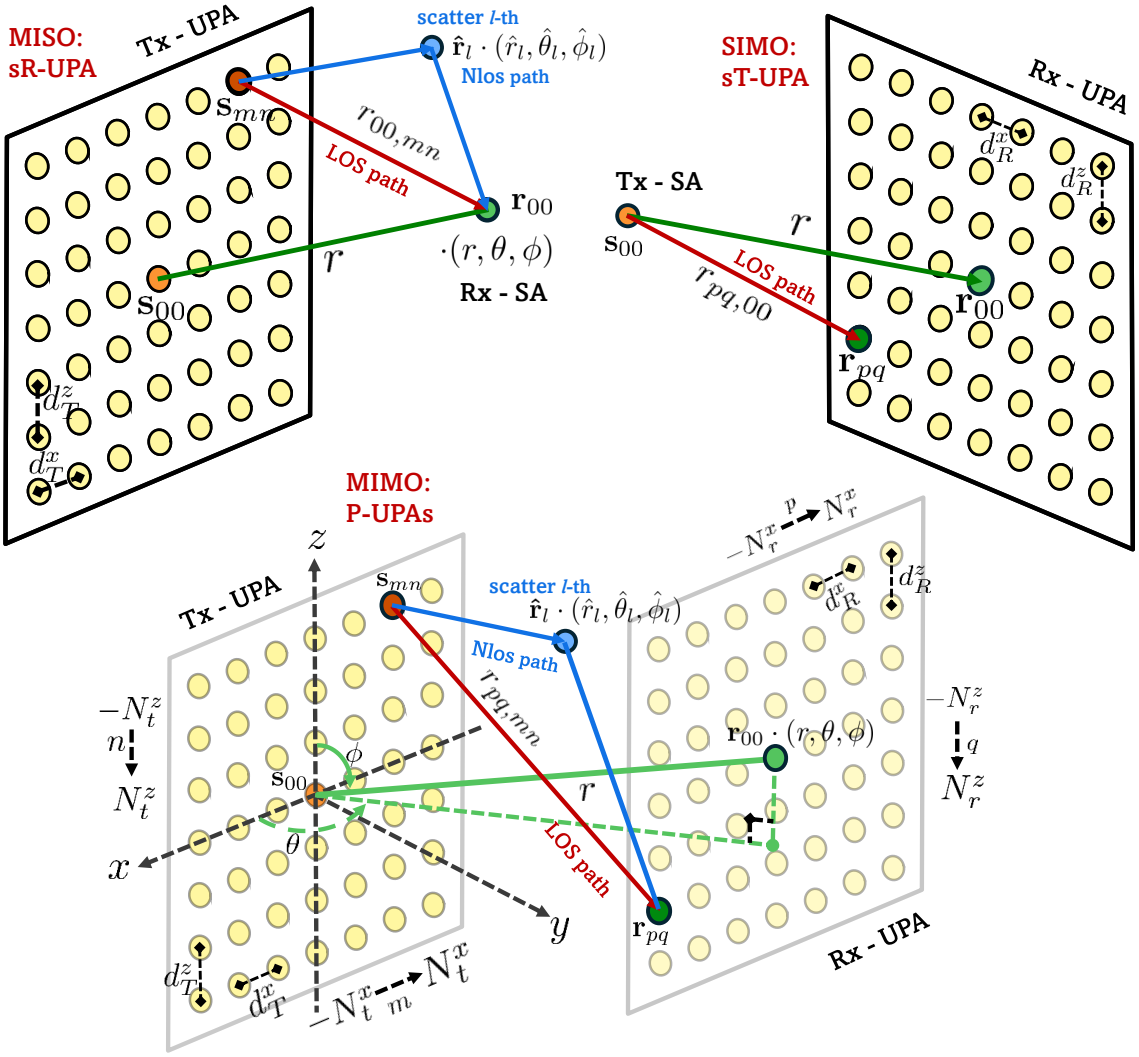

Figure 6. The layout coordinates of single-antenna UPA & Parallel UPAs system.

Substituting the phase decomposition into Eq. (A.1.24), the channel coefficient becomes

$$h(\mathbf{r}_{pq}, \mathbf{s}_{mn}) = \beta^*_{pq,mn} \exp(-j \cdot \phi_{pq,mn}) \qquad \text{(A.1.27)}$$
$$= \beta^*_{pq,mn} \cdot a^{\mathcal{T}}_{\text{UPA}}(\mathbf{r}_{00}, \mathbf{s}_{mn}) \cdot a^{\mathcal{R}}_{\text{UPA}}(\mathbf{r}_{pq}, \mathbf{s}_{00}) \cdot h^c_{pq,mn}$$

where the array response and coupling terms are defined as follows. The complex gain matrix $\boldsymbol{\beta}_* \in \mathbb{C}^{N_{\mathcal{R}} \times N_{\mathcal{T}}}$ takes $\beta^*_{pq,mn}$ as the element indexed by $(r; t)$:

$$(r;\, t) = (p \cdot N^z_{\mathcal{R}} + q;\; m \cdot N^z_{\mathcal{T}} + n), \qquad \text{(A.1.28a)}$$
$$\beta^*_{pq,mn} = [\boldsymbol{\beta}_*]_{r,t}$$
$$= \beta_{pq,mn} \exp\left(-j\tfrac{2\pi}{\lambda} r\right). \qquad \text{(A.1.28b)}$$

Following the separability of a 2D UPA, the Tx

Table 10. System parameters and coordinates of Tx & Rx UPA antenna elements.

Description	**Expression**
Number of Tx antennas	$N_{\mathcal{T}} = N_{\mathcal{T}}^x \times N_{\mathcal{T}}^z = (2N_t^x + 1) \times (2N_t^z + 1)$
Tx antenna indices	$m \in \{-N_t^x, \cdots, N_t^x\}, \quad n \in \{-N_t^z, \cdots, N_t^z\}$
Tx antenna spacing	d_T^x along Ox axis, $\quad d_T^z$ along Oz axis
Center Tx element	$\mathbf{s}_{00} = (0, 0, 0)$
(m, n)-th Tx element coordinate	$\mathbf{s}_{mn} = (md_T^x,\ 0,\ nd_T^z)$
Number of Rx antennas	$N_{\mathcal{R}} = N_{\mathcal{R}}^x \times N_{\mathcal{R}}^z = (2N_r^x + 1) \times (2N_r^z + 1)$
Rx antenna indices	$p \in \{-N_r^x, \cdots, N_r^x\}, \quad q \in \{-N_r^z, \cdots, N_r^z\}$
Rx antenna spacing	d_R^x along Ox axis, $\quad d_R^z$ along Oz axis
Center Rx element (spherical)	$\mathbf{r}_{00}(r, \theta, \phi) = (r\cos\theta\sin\phi,\ r\cos\theta\cos\phi,\ r\cos\phi)$
(p, q)-th Rx element coordinate	$\mathbf{r}_{pq} = (r\cos\theta\sin\phi - pd_R^x,\ r\cos\theta\cos\phi,\ r\cos\phi - qd_R^z)$
Distance between UPA centers	$r = \|\mathbf{r}_{00} - \mathbf{s}_{00}\|$
Link distance Tx-(m, n) to Rx-(p, q)	$r_{pq,mn} = \|\mathbf{r}_{pq} - \mathbf{s}_{mn}\|$

ARV $\mathbf{a}_{\text{UPA}}^{\mathcal{T}} \in \mathbb{C}^{N_{\mathcal{T}} \times 1}$ factorizes as

$$a_{\text{UPA}}^{\mathcal{T}}(\mathbf{r}_{00}, \mathbf{s}_{mn}) = \left[\mathbf{a}_{\text{UPA}}^{\mathcal{T}}(\mathbf{r}_{00}, \mathbf{s}_{00})\right]_t = a_{\text{UPA}}^{\mathcal{T}x}(\mathbf{r}_{00}, \mathbf{s}_{m0}) \cdot a_{\text{UPA}}^{\mathcal{T}z}(\mathbf{r}_{00}, \mathbf{s}_{0n}), \quad \text{(A.1.29a)}$$

$$\mathbf{a}_{\text{UPA}}^{\mathcal{T}}(\mathbf{r}_{00}, \mathbf{s}_{00}) \in \mathbb{C}^{N_{\mathcal{T}} \times 1} = \mathbf{a}_{\text{UPA}}^{\mathcal{T}x}(\mathbf{r}_{00}, \mathbf{s}_{00}) \otimes \mathbf{a}_{\text{UPA}}^{\mathcal{T}z}(\mathbf{r}_{00}, \mathbf{s}_{00}), \quad \text{(A.1.29b)}$$

where it is composed by the ARV along x– and z-axis as $\mathbf{a}_{\text{UPA}}^{\mathcal{T}x}(\mathbf{r}_{00}, \mathbf{s}_{00}) \in \mathbb{C}^{N_{\mathcal{T}}^x \times 1}$ and $\mathbf{a}_{\text{UPA}}^{\mathcal{T}z}(\mathbf{r}_{00}, \mathbf{s}_{00}) \in \mathbb{C}^{N_{\mathcal{T}}^z \times 1}$, respectively:

$$a_{\text{UPA}}^{\mathcal{T}x}(\mathbf{r}_{00}, \mathbf{s}_{m0}) = \left[\mathbf{a}_{\text{UPA}}^{\mathcal{T}x}(\mathbf{r}_{00}, \mathbf{s}_{00})\right]_m = \exp(-j\,\phi_{00,m0}), \quad \text{(A.1.30a)}$$

$$a_{\text{UPA}}^{\mathcal{T}z}(\mathbf{r}_{00}, \mathbf{s}_{0n}) = \left[\mathbf{a}_{\text{UPA}}^{\mathcal{T}z}(\mathbf{r}_{00}, \mathbf{s}_{00})\right]_n = \exp(-j\,\phi_{00,0n}). \quad \text{(A.1.30b)}$$

Similarly, $\mathbf{a}_{\text{UPA}}^{\mathcal{R}} \in \mathbb{C}^{N_{\mathcal{R}} \times 1}$ factorizes as

$$a_{\text{UPA}}^{\mathcal{R}}(\mathbf{r}_{pq}, \mathbf{s}_{00}) = \left[\mathbf{a}_{\text{UPA}}^{\mathcal{R}}(\mathbf{r}_{00}, \mathbf{s}_{00})\right]_r = a_{\text{UPA}}^{\mathcal{R}x}(\mathbf{r}_{p0}, \mathbf{s}_{00}) \cdot a_{\text{UPA}}^{\mathcal{R}z}(\mathbf{r}_{0q}, \mathbf{s}_{00}), \quad \text{(A.1.31a)}$$

$$\mathbf{a}_{\text{UPA}}^{\mathcal{R}}(\mathbf{r}_{00}, \mathbf{s}_{00}) \in \mathbb{C}^{N_{\mathcal{R}} \times 1} = \mathbf{a}_{\text{UPA}}^{\mathcal{R}x}(\mathbf{r}_{00}, \mathbf{s}_{00}) \otimes \mathbf{a}_{\text{UPA}}^{\mathcal{R}z}(\mathbf{r}_{00}, \mathbf{s}_{00}), \quad \text{(A.1.31b)}$$

where it is composed by the ARV along x– and z-axis as $\mathbf{a}_{\text{UPA}}^{\mathcal{R}x}(\mathbf{r}_{00}, \mathbf{s}_{00}) \in \mathbb{C}^{N_{\mathcal{R}}^x \times 1}$ and $\mathbf{a}_{\text{UPA}}^{\mathcal{R}z}(\mathbf{r}_{00}, \mathbf{s}_{00}) \in \mathbb{C}^{N_{\mathcal{R}}^z \times 1}$, respectively:

$$a_{\text{UPA}}^{\mathcal{R}x}(\mathbf{r}_{p0}, \mathbf{s}_{00}) = \left[\mathbf{a}_{\text{UPA}}^{\mathcal{T}x}(\mathbf{r}_{00}, \mathbf{s}_{00})\right]_p = \exp\left(-j\,\phi_{p0,00}\right), \quad \text{(A.1.32a)}$$

$$a_{\text{UPA}}^{\mathcal{R}z}(\mathbf{r}_{0q}, \mathbf{s}_{00}) = \left[\mathbf{a}_{\text{UPA}}^{\mathcal{T}z}(\mathbf{r}_{00}, \mathbf{s}_{00})\right]_q = \exp\left(-j\,\phi_{0q,00}\right). \quad \text{(A.1.32b)}$$

The coupling factor separates along x and z axes as

$$h_{pq,mn}^c = \left[\mathbf{H}^c\right]_{r,t} = h_{p,m}^{cx} \cdot h_{q,n}^{cz}, \quad \text{(A.1.33)}$$

$$\mathbf{H}^c = \mathbf{H}^{cx} \otimes \mathbf{H}^{cz} \in \mathbb{C}^{N_{\mathcal{R}} \times N_{\mathcal{T}}}, \quad \text{(A.1.34)}$$

where its coupling sub-matrices are denoted by $\mathbf{H}^{cx} \in \mathbb{C}^{N_{\mathcal{R}}^x \times N_{\mathcal{T}}^x}$ and $\mathbf{H}^{cz} \in \mathbb{C}^{N_{\mathcal{R}}^z \times N_{\mathcal{T}}^z}$. The full coupling matrix is

$$\left[\mathbf{H}^{cx}\right]_{p,m} = h_{p,m}^{cx} = \exp\left(-j \cdot \phi_{p,m}^{cx}\right), \quad \text{(A.1.35)}$$

$$\left[\mathbf{H}^{cz}\right]_{q,n} = h_{q,n}^{cz} = \exp\left(-j \cdot \phi_{q,n}^{cz}\right). \quad \text{(A.1.36)}$$

The LoS channel of Parallel UPAs system

$$\mathbf{H}_{\text{P-UPAs}}^{\text{LoS}} \in \mathbb{C}^{N_{\mathcal{R}} \times N_{\mathcal{T}}} = \boldsymbol{\beta}_* \odot \left(\mathbf{a}_{\text{UPA}}^{\mathcal{R}}(\mathbf{r}_{00}, \mathbf{s}_{00})\right)\left(\mathbf{a}_{\text{UPA}}^{\mathcal{T}}(\mathbf{r}_{00}, \mathbf{s}_{00})\right)^{\mathsf{T}} \odot \mathbf{H}^c. \quad \text{(A.1.37)}$$

A.1.2.2 Single-antenna and UPA - LoS channel

We first consider a MISO configuration where the receiver is equipped with a single antenna ($N_{\mathcal{R}} = 1$, i.e., $p = q = 0$), while the transmitter maintains a UPA. Using the phase decomposition in Eq. (A.1.25a), the channel coefficient between the (m, n)-th Tx element and the single Rx antenna simplifies to

$$\begin{aligned} h(\mathbf{r}_{00}, \mathbf{s}_{mn}) &= \beta^*_{00,mn} \exp(-j \cdot \phi_{00,mn}) \\ &= \beta^*_{00,mn} \cdot a^{\mathcal{T}}_{\text{UPA}}(\mathbf{r}_{00}, \mathbf{s}_{mn}), \end{aligned} \quad \text{(A.1.38)}$$

where $\beta^*_{00,mn}$ is the corresponding complex gain to $\beta_{00,mn}$ and $\boldsymbol{\beta}^{\mathcal{T}}_* \in \mathbb{C}^{N_{\mathcal{T}} \times 1}$ is the overall complex gain of UPA matrix at Tx can be computed as:

$$t = m \cdot N^z_{\mathcal{R}} + n, \quad \text{(A.1.39a)}$$

$$\beta^*_{00,mn} = \left[\boldsymbol{\beta}^{\mathcal{T}}_*\right]_t = \beta_{00,mn} \exp\left(-j\tfrac{2\pi}{\lambda} r\right). \quad \text{(A.1.39b)}$$

The LoS channel of sR-UPA system

$$\begin{aligned} \mathbf{H}^{\text{LoS}}_{\text{sR-UPA}} &= \mathbf{h}^{\mathcal{T}}_{\text{UPA}}(\mathbf{r}_{00}, \mathbf{s}_{00}) \in \mathbb{C}^{1 \times N_{\mathcal{T}}} \\ &= \left[\boldsymbol{\beta}^{\mathcal{T}}_* \odot \mathbf{a}^{\mathcal{T}}_{\text{UPA}}(\mathbf{r}_{00}, \mathbf{s}_{00})\right]^{\mathsf{T}}. \end{aligned} \quad \text{(A.1.40)}$$

Conversely, for a SIMO configuration where the transmitter has a single antenna ($N_{\mathcal{T}} = 1$, i.e., $m = n = 0$) and the receiver employs a UPA, the channel coefficient between the single Tx antenna and the (p, q)-th Rx element becomes

$$\begin{aligned} h(\mathbf{r}_{pq}, \mathbf{s}_{00}) &= \beta_{pq,00} \exp\!\left(-j\tfrac{2\pi}{\lambda} r\right) \exp\!\left(-j\phi_{pq,00}\right) \\ &= \beta^*_{pq,00} \cdot a^{\mathcal{R}}_{\text{UPA}}(\mathbf{r}_{pq}, \mathbf{s}_{00}), \end{aligned} \quad \text{(A.1.41)}$$

where $\beta^*_{pq,00}$ is the corresponding complex channel gain to $\beta^*_{pq,00}$ and the overall complex gain of UPA matrix at Tx can be computed as:

$$r = p \cdot N^z_{\mathcal{R}} + q, \quad \text{(A.1.42a)}$$

$$\beta^*_{pq,00} = \left[\boldsymbol{\beta}^{\mathcal{R}}_*\right]_r = \beta_{pq,00} \exp\left(-j\tfrac{2\pi}{\lambda} r\right). \quad \text{(A.1.42b)}$$

The LoS channel of sT-UPA system

$$\begin{aligned} \mathbf{H}^{\text{LoS}}_{\text{sT-UPA}} &= \mathbf{h}^{\mathcal{R}}_{\text{UPA}}(\mathbf{r}_{00}, \mathbf{s}_{00}) \in \mathbb{C}^{N_{\mathcal{R}} \times 1} \\ &= \boldsymbol{\beta}^{\mathcal{R}}_* \odot \mathbf{a}^{\mathcal{R}}_{\text{UPA}}(\mathbf{r}_{00}, \mathbf{s}_{00}). \end{aligned} \quad \text{(A.1.43)}$$

A.1.2.3 Multi-path channels

Consider an environment with $L - 1$ scatterers, each contributing an NLoS path via reflection. The l-th scatterer is located at $\hat{\mathbf{r}}_l$ with spherical coordinates $(\hat{r}_l, \hat{\theta}_l, \hat{\phi}_l)$. Following the cascade approach used for ULAs, the NLoS channel matrix for the l-th scatterer is

The NLoS channel of P-UPAs system

$$\begin{aligned} &\mathbf{H}^{\text{NLoS}}_{\text{P-UPAs}}(\mathbf{r}_{00}, \mathbf{s}_{00}, \hat{\mathbf{r}}_l) = \mathbf{h}^{\mathcal{R}}_{\text{UPA}}(\mathbf{r}_{00}, \hat{\mathbf{r}}_l)\, \mathbf{h}^{\mathcal{T}}_{\text{UPA}}(\hat{\mathbf{r}}_l, \mathbf{s}_{00}) \\ &= \left[\boldsymbol{\beta}^{\mathcal{R}}_{*,l} \odot \mathbf{a}^{\mathcal{R}}_{\text{UPA}}(\mathbf{r}_{00}, \hat{\mathbf{r}}_l)\right]\left[\boldsymbol{\beta}^{\mathcal{T}}_{*,l} \odot \mathbf{a}^{\mathcal{T}}_{\text{UPA}}(\hat{\mathbf{r}}_l, \mathbf{s}_{00})\right]^{\mathsf{T}} \\ &= \boldsymbol{\beta}_{*,l} \odot \left(\mathbf{a}^{\mathcal{R}}_{\text{UPA}}(\mathbf{r}_{00}, \hat{\mathbf{r}}_l)\right)\left(\mathbf{a}^{\mathcal{T}}_{\text{UPA}}(\hat{\mathbf{r}}_l, \mathbf{s}_{00})\right)^{\mathsf{T}}, \end{aligned} \quad \text{(A.1.44)}$$

where $\boldsymbol{\beta}_{*,l} = \left[\boldsymbol{\beta}^{\mathcal{R}}_{*,l}\right]\left[\boldsymbol{\beta}^{\mathcal{T}}_{*,l}\right]^{\mathsf{T}} \in \mathbb{C}^{N_{\mathcal{R}} \times N_{\mathcal{T}}}$ denotes the joint complex gain, where each is defined by the instruction in Eq. (A.1.39b), Eq. (A.1.42b).

Considering a MISO configuration where the receiver is equipped with a single antenna, the NLoS channel matrix computed for the l-th scatterer is

The NLoS channel of sR-UPA system

$$\mathbf{H}^{\text{NLoS}}_{\text{sR-UPA}} = \sum_{l=1}^{L} \left[\boldsymbol{\beta}^{\mathcal{T}}_{*,l} \odot \mathbf{a}^{\mathcal{T}}_{\text{UPA}}(\hat{\mathbf{r}}_l, \mathbf{s}_{00})\right]^{\mathsf{T}} \quad \text{(A.1.45)}$$

A.1.3 Amplitude Gain Modeling

The transition from far-field to near-field propagation is characterized by two key distance boundaries. RD governs the linearity of the phase across the array, the UPD defines the boundary beyond which signal amplitude can be considered

uniform across all antenna elements. Within the near-field region, amplitude variations become increasingly significant as the distance decreases below the UPD.

A.1.3.1 General modeling for power gain

The total channel power gain between a transmit antenna at position $\mathbf{s}$ and a receive antenna at $\mathbf{r}$ comprises three multiplicative factors, each capturing a distinct physical phenomenon.

First, the free-space path loss (FSPL) quantifies the attenuation of signal power as it propagates through a free-space environment, following the inverse-square law [122]. Based on the Friis transmission formula, the power gain due to free-space path loss for the link between $\mathbf{s}$ and $\mathbf{r}$ is given by:

$$G_0(\mathbf{r}, \mathbf{s}) = \frac{1}{4\pi \|\mathbf{r} - \mathbf{s}\|^2}, \tag{A.1.46}$$

where $\|\mathbf{r} - \mathbf{s}\|$ denotes the Euclidean distance between the transmit and receive antennas.

Second, the effective aperture loss (EAL) accounts for the angular misalignment between the incident wave and the antenna's maximum effective aperture. Assuming an ideal isotropic receiver with maximum effective aperture $A_e = \lambda^2/(4\pi)$ and letting $\hat{\mathbf{u}}_s$ denote the unit vector normal to the transmit aperture, the gain factor is

$$G_1(\mathbf{r}, \mathbf{s}) = \frac{(\mathbf{r} - \mathbf{s})^\mathsf{T} \hat{\mathbf{u}}_s}{\|\mathbf{r} - \mathbf{s}\| \cdot \|\hat{\mathbf{u}}_s\|}, \tag{A.1.47}$$

where $\|\hat{\mathbf{u}}_s\| = 1$ is unit norm. For a transmit array lying in the xz-plane, then $\hat{\mathbf{u}}_s = [0, 1, 0]^\mathsf{T}$, aligned with the y-axis. Here, $G_1 = 1$ for perpendicular incidence and $G_1 = 0$ for tangential incidence.

Third, the polarization loss (PL) arises from a mismatch between the polarization of the incident wave and the receive antenna. Let ϕ be the angle between the receive antenna polarization vector and the incoming wave's polarization. The polarization gain can be expressed as

$$G_2(\mathbf{r}, \mathbf{s}) = \frac{|\boldsymbol{\rho}_w^\mathsf{T}(\mathbf{r}) \mathbf{e}(\mathbf{r}, \mathbf{s})|^2}{\|\boldsymbol{\rho}_w^\mathsf{T}(\mathbf{r})\|^2 \|\mathbf{e}(\mathbf{r}, \mathbf{s})\|^2}, \tag{A.1.48a}$$

$$\mathbf{e}(\mathbf{r}, \mathbf{s}) = \left(\mathbf{I} - \frac{(\mathbf{r} - \mathbf{s})(\mathbf{r} - \mathbf{s})^\mathsf{T}}{\|\mathbf{r} - \mathbf{s}\|^2} \right) \hat{\mathbf{J}}(\mathbf{s}), \tag{A.1.48b}$$

where $\boldsymbol{\rho}_w(\mathbf{r})$ is the normalized receiving-mode polarization vector ($\|\boldsymbol{\rho}_w(\mathbf{r})\| = 1$), $\mathbf{e}(\mathbf{r}, \mathbf{s})$ is the polarization vector of the incident wave, and $\hat{\mathbf{J}}(\mathbf{s})$ is the normalized electric current vector at the transmitter.

General Amplitude Gain Expression: Combining the above factors, the overall channel amplitude gain $\beta(\mathbf{r}, \mathbf{s})$ is given by the square root of the total channel power gain:

$$\begin{aligned} \beta(\mathbf{r}, \mathbf{s}) &= \sqrt{G_0(\mathbf{r}, \mathbf{s}) G_1(\mathbf{r}, \mathbf{s}) G_2(\mathbf{r}, \mathbf{s})} \\ &= \sqrt{\frac{G_1(\mathbf{r}, \mathbf{s}) G_2(\mathbf{r}, \mathbf{s})}{4\pi \|\mathbf{r} - \mathbf{s}\|^2}}. \end{aligned} \tag{A.1.49}$$

The maximum gain occurs when $G_1 = G_2 = 1$, i.e., perpendicular incidence with perfect polarization matching. In this ideal scenario, the channel gain is limited solely by free-space path loss.

A.1.3.2 Uniform and Non-uniform Power Spherical Wave

For a MIMO system with transmit and receive arrays, the amplitude gain for the link between the n-th Tx antenna and m-th Rx antenna is

$$\beta_{m,n}(r) = \sqrt{\frac{G_1(\mathbf{s}_n, \mathbf{r}_m) G_2(\mathbf{s}_n, \mathbf{r}_m)}{4\pi \|\mathbf{r}_m - \mathbf{s}_n\|^2}}, \tag{A.1.50}$$

where the distance between the reference points of two antenna arrays is denoted by r. The UPD is defined as the minimum distance satisfying a prescribed uniformity threshold Γ as

$$r_{\text{UPD}} = \arg\min_r r, \quad \text{s.t.} \ \frac{\min_{m,n} \beta_{m,n}(r)}{\max_{p,q} \beta_{p,q}(r)} \geq \Gamma. \tag{A.1.51}$$

When the effects of effective aperture loss and polarization loss are neglected (i.e., $G_1 G_2 = 1$),

the amplitude gain simplifies to a function of distance only as FSPL. This yields two distinct models as

$$\beta_{m,n}^{\mathrm{NUSW}} = \frac{1}{\sqrt{4\pi\|\mathbf{r}_m - \mathbf{s}_n\|^2}}, \tag{A.1.52a}$$

$$\beta_{m,n}^{\mathrm{USW}} = \frac{1}{\sqrt{4\pi r^2}}. \tag{A.1.52b}$$

The USW model is valid beyond the UPD, a regime where amplitude variations across the large-scale array become negligible, allowing for a simplified phase-only near-field characterization. Conversely, between the Fresnel distance and the UPD, the NUSW model must be employed to accurately capture the distance-dependent amplitude fluctuations inherent to the radiating near-field. Below the Fresnel boundary, within the reactive near-field, EM fields exhibit highly complex, non-propagating behavior; however, this region is typically omitted from communication frameworks due to the evanescent nature of the waves and their rapid spatial decay.

Appendix A.2 Derived Rayleigh Distances

For simplicity, a uniform linear array (ULA) configuration is adopted to analyze both multiple-input single-output (MISO) and multiple-input multiple-output (MIMO) systems, as depicted in Figure 7.

In the MISO setup, the transmitter employs a ULA, whereas the receiver is modeled as a single-antenna receiver. In contrast, the MIMO configuration assumes parallel ULAs at both the transmitter and receiver, thereby facilitating a simplified characterization of multi-antenna system performance.

A.2.1 MISO Rayleigh Distance

The propagation phase and propagation distance of sR-ULA system can be computed as follows:

$$\begin{aligned} r_n &= \|\mathbf{r}_0 - \mathbf{s}_n\| = \dots \\ &= r\sqrt{1 + \frac{-2nd\cos\theta}{r} + \frac{(nd)^2}{r^2}} && \text{(A.2.1a)} \\ &\overset{(2)}{\approx} r - nd\sin\theta + \frac{n^2d^2\cos^2\theta}{2r} && \text{(A.2.1b)} \end{aligned}$$

$$\begin{aligned} \phi_n &= \frac{2\pi}{\lambda}(r_n - r) && \text{(A.2.2a)} \\ &\overset{(2)}{\approx} \frac{-2\pi d\sin\theta}{\lambda}n + \frac{\pi d^2\cos^2\theta}{\lambda r}n^2, && \text{(A.2.2b)} \\ \phi_n^{\mathrm{near}} &= \phi_n^{\mathrm{far}} + \Delta_n^{\phi}, && \text{(A.2.2c)} \end{aligned}$$

where the symbol $\overset{(2)}{\approx}$ denotes the second-order Taylor expansion.

In this context, the far-field phase ϕ_n^{far} can be approximated by retaining only the first-order term of the expansion, which ensures a linear phase variation across array elements. The classical Rayleigh distance is then defined as the minimum distance at which this linear approximation remains sufficiently accurate, specifically by requiring that the maximum phase error Δ_n^{ϕ} introduced by neglecting higher-order terms does not exceed $\pi/8$. With the antenna aperture $D = (N_{\mathcal{T}} - 1)d = 2N_t d$, and angle $\cos^2\theta \in [0; 1]$, , the corresponding expression of Δ_n^{ϕ} leads to:

$$\begin{aligned} n &= -N_t, \dots, N_t && \text{(A.2.3a)} \\ \max_{n,\theta} \Delta_n^{\phi} &= \frac{1}{r}\frac{\pi n^2 d^2}{\lambda}\cos^2\theta = \frac{\pi}{8} && \text{(A.2.3b)} \\ \Longleftrightarrow r &= \max_{n,\theta} \frac{8(nd)^2\cos^2\theta}{\lambda}. && \text{(A.2.3c)} \\ R_D &\triangleq \frac{2D^2}{\lambda}. && \text{(A.2.3d)} \end{aligned}$$

In contrast, the more recent notion of the Effective Rayleigh Distance (ERD) characterizes the near-field range in terms of beamforming

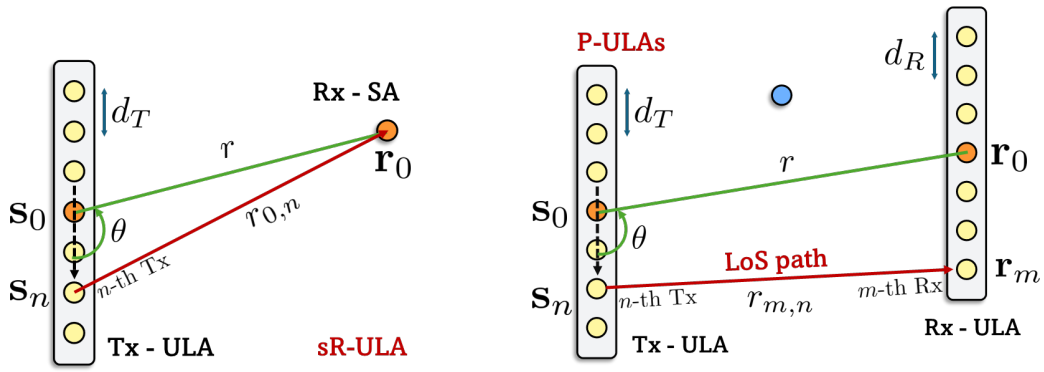

Figure 7. The layout of system MISO-ULA and MIMO-ULA.

gain degradation ϵ rather than phase curvature alone. Specifically, ERD introduces a non-uniform boundary that depends on the azimuth angle θ, reflecting the fact that beam focusing capability varies across spatial directions. The illustration for this metric is depicted as in Figure 8.

$$\max_n \Delta_n^{\phi} = \frac{1}{r}\frac{\pi n^2 d^2}{\lambda}\cos^2\theta = \frac{\pi}{8} \tag{A.2.4a}$$

$$\iff r = \max_n \frac{8(nd)^2}{\lambda}\cos^2\theta \tag{A.2.4b}$$

$$= \frac{2D^2}{\lambda}\cos^2\theta = R_D\cos^2\theta \tag{A.2.4c}$$

$$R_{ER} \triangleq \epsilon \cdot R_D\cos^2\theta \tag{A.2.4d}$$

A.2.2 MIMO Rayleigh Distance

Adopting the derivation from the manuscript, the near-field propagation phase $\phi_{m,n}$ in this MIMO setting could be computed as:

$$\phi_{m,n}^{\text{near}} = \phi_{0,n} + \phi_{m,0} + \phi_{m,n}^{c} \tag{A.2.5a}$$

$$\phi_{m,n}^{c} = \frac{2\pi}{\lambda}\frac{nd_T \cdot md_R\sin^2\theta}{r} \tag{A.2.5b}$$

Here, D_T and D_R are denoted for the antenna apertures of Tx and Rx arrays, respectively. Within the range of the antenna indices defined as:

$$m = -N_r, \ldots, N_r \tag{A.2.6a}$$

$$n = -N_t, \ldots, N_t \tag{A.2.6b}$$

$$D_T = 2N_t d_t \tag{A.2.6c}$$

$$D_R = 2N_r d_r \tag{A.2.6d}$$

The Rayleigh distance in MIMO system can be computed as:

$$\max_{m,n,\theta} \Delta_{m,n}^{\phi} = \frac{1}{r}\frac{\pi(nd_T + md_R)^2\sin^2\theta}{\lambda} = \frac{\pi}{8}, \tag{A.2.7a}$$

$$\iff r = \max_{m,n,\theta}\frac{8(nd_T + md_R)^2\cos^2\theta}{\lambda}. \tag{A.2.7b}$$

$$R_D^{\text{MIMO}} \triangleq \frac{2(D_T + D_R)^2}{\lambda}. \tag{A.2.7c}$$

The Effective Rayleigh distance in MIMO system can be extended from the work [59], where ϵ denotes for pre-definied beamforming gain:

$$\max_{m,n} \Delta_{m,n}^{\phi} = \frac{1}{r}\frac{\pi(nd_T + md_R)^2\sin^2\theta}{\lambda} = \frac{\pi}{8}, \tag{A.2.8a}$$

$$\iff r = \max_{m,n}\frac{8(nd_T + md_R)^2\cos^2\theta}{\lambda} \tag{A.2.8b}$$

$$= \frac{2(D_T + D_R)^2}{\lambda}\cos^2\theta \tag{A.2.8c}$$

$$R_{ER}^{\text{MIMO}} \triangleq \epsilon \cdot \frac{2(D_T + D_R)^2}{\lambda}\cos^2\theta \tag{A.2.8d}$$

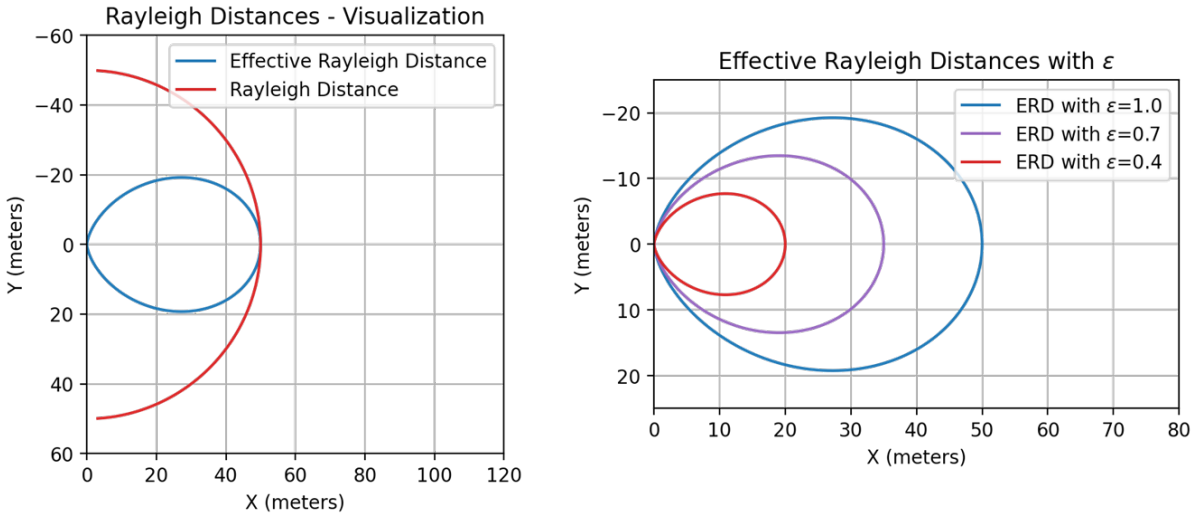

Figure 8. The illustration of Rayleigh Distance and Effective Rayleigh Distance.

The definition of Advanced MIMO Rayleigh distance - R_{AD}^{MIMO} is proposed by work [52].

$$\max_{m,n,\theta} \phi_{m,n}^{c} = \frac{1}{r}\frac{2\pi n d_T \cdot m d_R \sin^2\theta}{\lambda} = \frac{\pi}{8}, \quad \text{(A.2.9a)}$$

$$\Longleftrightarrow \quad r = \max_{m,n,\theta} \frac{16 \cdot n d_T \cdot m d_R \sin^2\theta}{\lambda} \quad \text{(A.2.9b)}$$

$$R_{AD}^{\text{MIMO}} \triangleq \frac{4 D_T D_R}{\lambda}. \quad \text{(A.2.9c)}$$

References

[1] S. A. Abdel Hakeem, H. H. Hussein, H. Kim, Vision and Research Directions of 6G Technologies and Applications, Journal of King Saud University - Computer and Information Sciences, Vol. 34, No. 6, Part A, 2022, pp. 2419–2442. https://doi.org/10.1016/j.jksuci.2022.03.019.

[2] C.-X. Wang, X. You, X. Gao, X. Zhu, Z. Li, C. Zhang, H. Wang, Y. Huang, Y. Chen, H. Haas, J. S. Thompson, E. G. Larsson, M. D. Renzo, W. Tong, P. Zhu, X. Shen, H. V. Poor, L. Hanzo, On the Road to 6G: Visions, Requirements, Key Technologies, and Testbeds, IEEE Communications Surveys & Tutorials, Vol. 25, No. 2, 2023, pp. 905–974. https://doi.org/10.48550/arXiv.2302.14536.

[3] S. Abdel Hakeem, H. Hussein, H. Kim, Security Requirements and Challenges of 6G Technologies and Applications, Sensors, Vol. 22, 2022, pp. 1969. https://doi.org/10.3390/s22051969.

[4] Y. Zhao, L. Dai, J. Zhang, A. Elzanaty, V. Monzon Baeza, 6G Near-Field Technologies White Paper, FuTURE Forum, 2024.

[5] International Telecommunication Union, Radiocommunication Sector (ITU-R), Framework and Overall Objectives of the Future Development of IMT for 2030 and Beyond, Recommendation Recommendation ITU-R M.2160-0, ITU-R (Nov 2023).

[6] W. Saad, M. Bennis, M. Chen, A Vision of 6G Wireless Systems: Applications, Trends, Technologies, and Open Research Problems, IEEE Network, Vol. 34, No. 3, 2020, pp. 134–142. https://doi.org/10.1109/MNET.001.1900287.

[7] R. Chataut, M. Nankya, R. Akl, 6G Networks and the AI Revolution—Exploring Technologies, Applications, and Emerging Challenges, Sensors, Vol. 24, 2024, pp. 1888. https://doi.org/10.3390/s24061888.

[8] S. Alraih, I. Shayea, M. Behjati, R. Nordin, N. Abdullah, A. Abu-Samah, D. Nandi, Revolution or Evolution? Technical Requirements and Considerations Towards 6G Mobile Communications, Sensors, Vol. 22, 2022, pp. 762. https://doi.org/10.3390/s22030762.

[9] H. Zhang, N. Shlezinger, F. Guidi, D. Dardari, Y. C. Eldar, 6G Wireless Communications: From Far-Field Beam Steering to Near-Field Beam Focusing, IEEE Communications Magazine, Vol. 61, No. 4, 2023, pp. 72–77. https://doi.org/10.1109/MCOM.001.2200259.

[10] S. Ye, M. Xiao, M.-W. Kwan, Z. Ma, Y. Huang, G. Karagiannidis, P. Fan, Extremely Large Aperture Array (ELAA) Communications: Foundations, Research Advances and Challenges, IEEE Open Journal of the Communications Society, Vol. 5, 2024, pp. 7075–7120. https://doi.org/10.1109/OJCOMS.2024.3486172.

[11] A. Paulraj, D. Gore, R. Nabar, H. Bolcskei, An Overview of MIMO Communications - A Key to Gigabit Wireless, Proceedings of the IEEE, Vol. 92, No. 2, 2004, pp. 198–218. https://doi.org/10.1109/JPROC.2003.821915.

[12] Z. Wang, J. Zhang, H. Du, D. Niyato, S. Cui, B. Ai, M. Debbah, K. B. Letaief, H. V. Poor, A Tutorial on Extremely Large-Scale MIMO for 6G: Fundamentals, Signal Processing, and Applications, IEEE Communications Surveys & Tutorials, Vol. 26, No. 3, 2024, pp. 1560–1605. https://doi.org/10.1109/COMST.2023.3349276.

[13] H. Sarieddeen, M.-S. Alouini, T. Y. Al-Naffouri, An Overview of Signal Processing Techniques for Terahertz Communications, Proceedings of the IEEE, Vol. 109, No. 10, 2021, pp. 1628–1665. https://doi.org/10.1109/JPROC.2021.3100811.

[14] C. Lin, G. Y. L. Li, Terahertz Communications: An Array-of-Subarrays Solution, IEEE Communications Magazine, Vol. 54, No. 12, 2016, pp. 124–131. https://doi.org/10.1109/MCOM.2016.1600306CM.

[15] Y. Zhao, L. Dai, J. Zhang, R. Ji, M. Jian, H. Xue, H. Yu, Y. Sun, Y. Lu, Z. Wu, Z. Xu, J. Li, H. Miao, Z. Yuan, P. Tang, J. Shen, T. Gong, H. Liu, J. Han, Q. Feng, Z. Chen, L. Li, G. Yang, Y. Zeng, C. Pan, W. Liu, K. Zhi, W. Hu, Y. Liu, X. Mu, C. Yuen, M. Debbah, C. Huang, L. Li, P. Zhang, Near-Field Communications: Characteristics, Technologies, and Engineering, Frontiers of Information Technology & Electronic Engineering, Vol. 25, No. 12, 2024, pp. 1580–1626.

[16] S. Sun, R. Li, C. Han, X. Liu, L. Xue, M. Tao, How to Differentiate Between Near Field and Far Field: Revisiting the Rayleigh Distance, IEEE Communications Magazine, Vol. 63, No. 1, 2025, pp. 22–28. https://doi.org/10.1109/MCOM.001.2400007.

[17] J. Kraus, R. Marhefka, Antennas for All Applications, McGraw-Hill series in electrical engineering, McGraw-Hill, 2002.

[18] V. Arun, H. Balakrishnan, RFocus: Beamforming Using Thousands of Passive Antennas, in: 17th USENIX Symposium on Networked Systems Design and Implementation (NSDI 20), USENIX Association, Santa Clara, CA, 2020, pp. 1047–1061.

[19] D. A. B. Miller, Waves, Modes, Communications, and Optics: A Tutorial, Adv. Opt. Photon., Vol. 11, No. 3, 2019, pp. 679–825. https://doi.org/10.1364/AOP.11.000679.

[20] N. Decarli, D. Dardari, Communication Modes with Large Intelligent Surfaces in the Near Field, IEEE Access, Vol. 9, 2021, pp. 165648–165666. https://doi.org/10.1109/ACCESS.2021.3133707.

[21] H. Zhang, N. Shlezinger, F. Guidi, D. Dardari, M. F. Imani, Y. C. Eldar, Beam Focusing for Near-Field Multiuser MIMO Communications, IEEE Transactions on Wireless Communications, Vol. 21, No. 9, 2022, pp. 7476–7490. https://doi.org/10.1109/TWC.2022.3158894.

[22] S. Kim, J. Moon, J. Wu, B. Shim, M. Z. Win, Vision-Aided Positioning and Beam Focusing for 6G Terahertz Communications, IEEE Journal on Selected Areas in Communications, Vol. 42, No. 9, 2024, pp. 2503–2519. https://doi.org/10.1109/JSAC.2024.3413949.

[23] Z. Wu, L. Dai, Multiple Access for Near-Field Communications: SDMA or LDMA?, IEEE Journal on Selected Areas in Communications, Vol. 41, No. 6, 2023, pp. 1918–1935. https://doi.org/10.1109/JSAC.2023.3275616.

[24] Z. Wu, L. Dai, Location Division Multiple Access for Near-Field Communications, in: ICC 2023 - IEEE International Conference on Communications, 2023, pp. 2252–2257. https://doi.org/10.48550/arXiv.2301.09082.

[25] J. Duan, J. Hou, Physical Layer Security in NFC: Advances, Potential Toward 6G Wireless Communications, IEEE Network, Vol. 39, No. 6, 2025, pp. 48–53. https://doi.org/10.1109/MNET.2025.3599326.

[26] Y. Liu, J. Xu, Z. Wang, X. Mu, L. Hanzo, Near-Field Communications: What Will Be Different?, IEEE Wireless Communications, Vol. 32, No. 2, 2025, pp. 262–270. https://doi.org/10.1109/MWC.001.2300588.

[27] M. Cui, Z. Wu, Y. Lu, X. Wei, L. Dai, Near-Field MIMO Communications for 6G: Fundamentals, Challenges, Potentials, and Future Directions, IEEE Communications Magazine, Vol. 61, No. 1, 2023, pp. 40–46. https://doi.org/10.1109/MCOM.004.2200136.

[28] D. Serghiou, M. Khalily, T. W. C. Brown, R. Tafazolli, Terahertz Channel Propagation Phenomena, Measurement Techniques and Modeling for 6G Wireless Communication Applications: A Survey, Open Challenges and Future Research Directions, IEEE Communications Surveys & Tutorials, Vol. 24, No. 4, 2022, pp. 1957–1996. https://doi.org/10.1109/COMST.2022.3205505.

[29] C.-X. Wang, Z. Lv, X. Gao, X. You, Y. Hao, H. Haas, Pervasive Wireless Channel Modeling Theory and Applications to 6G GBSMs for All Frequency Bands and All Scenarios, IEEE Transactions on Vehicular Technology, Vol. 71, No. 9, 2022, pp. 9159–9173.

https://doi.org/10.1109/TVT.2022.3179695.

[30] Z. Wang, J. Zhang, H. Du, W. E. I. Sha, B. Ai, D. Niyato, M. Debbah, Extremely Large-Scale MIMO: Fundamentals, Challenges, Solutions, and Future Directions, IEEE Wireless Communications, Vol. 31, No. 3, 2024, pp. 117–124. https://doi.org/10.1109/MWC.132.2200443.

[31] H. Lu, Y. Zeng, C. You, Y. Han, J. Zhang, Z. Wang, Z. Dong, S. Jin, C.-X. Wang, T. Jiang, X. You, R. Zhang, A Tutorial on Near-Field XL-MIMO Communications Toward 6G, IEEE Communications Surveys & Tutorials, Vol. 26, No. 4, 2024, pp. 2213–2257. https://doi.org/10.1109/COMST.2024.3387749.

[32] Y. Liu, C. Ouyang, Z. Wang, J. Xu, X. Mu, A. L. Swindlehurst, Near-Field Communications: A Comprehensive Survey, IEEE Communications Surveys & Tutorials, Vol. 27, No. 3, 2025, pp. 1687–1728. https://doi.org/10.1109/COMST.2024.3475884.

[33] Y. Liu, Z. Wang, J. Xu, C. Ouyang, X. Mu, R. Schober, Near-Field Communications: A Tutorial Review, IEEE Open Journal of the Communications Society, Vol. 4, 2023, pp. 1999–2049. https://doi.org/10.1109/OJCOMS.2023.3305583.

[34] Z. Zhang, R. He, B. Ai, M. Yang, Y. Niu, Z. Zhong, Y. Li, X. Zhang, J. Li, A Cluster-Based Statistical Channel Model for Integrated Sensing and Communication Channels, IEEE Transactions on Wireless Communications, Vol. 23, No. 9, 2024, pp. 11597–11611. https://doi.org/10.1109/TWC.2024.3383594.

[35] T. Liu, K. Guan, D. He, P. T. Mathiopoulos, K. Yu, Z. Zhong, M. Guizani, 6G Integrated Sensing and Communications Channel Modeling: Challenges and Opportunities, IEEE Vehicular Technology Magazine, Vol. 19, No. 2, 2024, pp. 31–40. https://doi.org/10.1109/MVT.2024.3373930.

[36] Z. Wan, J. Zhu, L. Dai, Near-Field Channel Modeling for Electromagnetic Information Theory, IEEE Transactions on Wireless Communications, Vol. 23, No. 12, 2024, pp. 18004–18018. https://doi.org/10.1109/TWC.2024.3459006.

[37] J. Zhang, J. Lin, P. Tang, Y. Zhang, H. Xu, T. Gao, H. Miao, H. Gong, C. Zhao, Y. Liu, Y. Cai, Z. Yuan, L. Tian, S. Yang, L. Xia, G. Liu, P. Zhang, 6G Channel Modeling: Requirement, Measurement, Methodology and Simulator (2025). arXiv:2305.16616, https://doi.org/10.48550/arXiv.2305.16616.

[38] R. He, N. D. Cicco, B. Ai, M. Yang, Y. Miao, M. Boban, COST CA20120 INTERACT Framework of Artificial Intelligence-Based Channel Modeling, IEEE Wireless Communications, Vol. 32, No. 4, 2025, pp. 200–207. https://doi.org/10.1109/MWC.010.2400253.

[39] J. An, C. Yuen, C. Huang, M. Debbah, H. Vincent Poor, L. Hanzo, A Tutorial on Holographic MIMO Communications—Part I: Channel Modeling and Channel Estimation, IEEE Communications Letters, Vol. 27, No. 7, 2023, pp. 1664–1668. https://doi.org/10.1109/LCOMM.2023.3278683.

[40] N. Dreyer, T. Kürner, A Comparison of Stochastic and Deterministic Channel Models for V2V Applications, in: 2020 European Conference on Networks and Communications (EuCNC), 2020, pp. 79–83. https://doi.org/10.1109/EuCNC48522.2020.9200903.

[41] M. Patzold, U. Killat, F. Laue, Y. Li, On the Statistical Properties of Deterministic Simulation Models for Mobile Fading Channels, IEEE Transactions on Vehicular Technology, Vol. 47, No. 1, 1998, pp. 254–269. https://doi.org/10.1109/25.661052.

[42] T. Sarkar, H. Schwarzlander, S. Choi, M. Palma, M. Wicks, Stochastic Versus Deterministic Models in the Analysis of Communication Systems, IEEE Antennas and Propagation Magazine, Vol. 44, No. 4, 2002, pp. 40–50. https://doi.org/10.1109/MAP.2002.1043146.

[43] W. Jiang, Q. Zhou, J. He, M. A. Habibi, S. Melnyk, M. El-Absi, B. Han, M. D. Renzo, H. D. Schotten, F.-L. Luo, T. S. El-Bawab, M. Juntti, M. Debbah, V. C. M. Leung, Terahertz Communications and Sensing for 6G and Beyond: A Comprehensive Review, IEEE Communications Surveys & Tutorials, Vol. 26, No. 4, 2024, pp. 2326–2381. https://doi.org/10.1109/COMST.2024.3385908.

[44] Q. Xue, C. Ji, S. Ma, J. Guo, Y. Xu, Q. Chen, W. Zhang, A Survey of Beam Management for mmWave and THz Communications Towards 6G, IEEE Communications Surveys & Tutorials, Vol. 26, No. 3, 2024, pp. 1520–1559. https://doi.org/10.1109/COMST.2024.3361991.

[45] C.-X. Wang, Z. Lv, Y. Chen, H. Haas, A Complete Study of Space-Time-Frequency Statistical Properties of the 6G Pervasive Channel Model, IEEE Transactions on Communications, Vol. 71, No. 12, 2023, pp. 7273–7287. https://doi.org/10.1109/TCOMM.2023.3307144.

[46] K. Zhi, C. Pan, H. Ren, K. K. Chai, C.-X. Wang, R. Schober, X. You, Performance Analysis and Low-Complexity Design for XL-MIMO with Near-Field Spatial Non-Stationarities, IEEE Journal on Selected Areas in Communications, Vol. 42, No. 6, 2024, pp. 1656–1672. https://doi.org/10.1109/JSAC.2024.3389128.

[47] B. Di, Y. Zhang, R. Deng, M. Wang, S. Sun, L. Song, Holographic Metasurfaces for Extremely Large-Scale MIMO Communications: Design, Implementation, and Experiment Results, IEEE Wireless Communications 2025, pp. 1–8https://doi.org/10.1109/MWC.2025.3625029.

[48] Y. Liu, J. Zhang, Y. Zhang, Z. Yuan, G. Liu, A

Shared Cluster-Based Stochastic Channel Model for Integrated Sensing and Communication Systems, IEEE Transactions on Vehicular Technology, Vol. 73, No. 5, 2024, pp. 6032–6044. https://doi.org/10.1109/TVT.2023.3337648.

[49] M. D. Renzo, M. D. Migliore, Electromagnetic Signal and Information Theory, IEEE BITS the Information Theory Magazine, Vol. 4, No. 1, 2024, pp. 25–39. https://doi.org/10.1109/MBITS.2024.3359523.

[50] Q. Ma, J. Huang, Y. Yang, C.-X. Wang, J. Li, Degree of Freedom and Channel Capacity Studies of Near-Field Holographic MIMO, in: 2024 IEEE 24th International Conference on Communication Technology (ICCT), 2024, pp. 1622–1626. https://doi.org/10.1109/ICCT62411.2024.10946322.

[51] M. Cui, L. Dai, Channel Estimation for Extremely Large-Scale MIMO: Far-Field or Near-Field?, IEEE Transactions on Communications, Vol. 70, No. 4, 2022, pp. 2663–2677. https://doi.org/10.48550/arXiv.2108.07581.

[52] Y. Lu, L. Dai, Near-Field Channel Estimation in Mixed LoS/NLoS Environments for Extremely Large-Scale MIMO Systems, IEEE Transactions on Communications, Vol. 71, No. 6, 2023, pp. 3694–3707. https://doi.org/10.1109/TCOMM.2023.3260242.

[53] X. Wei, L. Dai, Channel Estimation for Extremely Large-Scale Massive MIMO: Far-Field, Near-Field, or Hybrid-Field?, IEEE Communications Letters, Vol. 26, No. 1, 2022, pp. 177–181. https://doi.org/10.1109/LCOMM.2021.3124927.

[54] V. T. Lam, D. H. Son, T. T. T. Quynh, T. T. Le, RACNN: Residual Attention Convolutional Neural Network for Near-Field Channel Estimation in 6G Wireless Communications, in: The 14th Conference on Information Technology and its Applications, Springer Nature Switzerland, Cham, 2026, pp. 387–399. https://doi.org/10.48550/arXiv.2503.02299.

[55] Y. Chen, L. Dai, Non-Stationary Channel Estimation for Extremely Large-Scale MIMO, IEEE Transactions on Wireless Communications, Vol. 23, No. 7, 2024, pp. 7683–7697. https://doi.org/10.1109/TWC.2023.3343740.

[56] Z. Dong, Y. Zeng, Near-Field Spatial Correlation for Extremely Large-Scale Array Communications, IEEE Communications Letters, Vol. 26, No. 7, 2022, pp. 1534–1538. https://doi.org/10.1109/LCOMM.2022.3170735.

[57] Y. Han, S. Jin, C.-K. Wen, X. Ma, Channel Estimation for Extremely Large-Scale Massive MIMO Systems, IEEE Wireless Communications Letters, Vol. 9, No. 5, 2020, pp. 633–637. https://doi.org/10.1109/LWC.2019.2963877.

[58] H. Luo, F. Gao, W. Yuan, S. Zhang, Beam Squint Assisted User Localization in Near-Field Integrated Sensing and Communications Systems, IEEE Transactions on Wireless Communications, Vol. 23, No. 5, 2024, pp. 4504–4517. https://doi.org/10.1109/TWC.2023.3319474.

[59] M. Cui, L. Dai, Near-Field Wideband Beamforming for Extremely Large Antenna Arrays, IEEE Transactions on Wireless Communications, Vol. 23, No. 10, 2024, pp. 13110–13124. https://doi.org/10.1109/TWC.2024.3398770.

[60] M. Cui, L. Dai, Z. Wang, S. Zhou, N. Ge, Near-Field Rainbow: Wideband Beam Training for XL-MIMO, IEEE Transactions on Wireless Communications, Vol. 22, No. 6, 2023, pp. 3899–3912. https://doi.org/10.1109/TWC.2022.3222198.

[61] H. Lei, J. Zhang, Z. Wang, B. Ai, D. W. Kwan Ng, Hybrid-Field Channel Estimation for XL-MIMO Systems with Stochastic Gradient Pursuit Algorithm, IEEE Transactions on Signal Processing, Vol. 72, 2024, pp. 2998–3012. https://doi.org/10.48550/arXiv.2405.15345.

[62] K. Chen, C. Qi, O. A. Dobre, G. Ye Li, Triple-Refined Hybrid-Field Beam Training for mmWave Extremely Large-Scale MIMO, IEEE Transactions on Wireless Communications, Vol. 23, No. 8, 2024, pp. 8556–8570. https://doi.org/10.1109/TWC.2024.3351712.

[63] Y. Chen, H. Shen, C. Han, Cross Far- and Near-Field Beam Management Technologies in Millimeter-Wave and Terahertz MIMO Systems, IEEE Open Journal of Vehicular Technology, Vol. 7, 2026, pp. 73–107. https://doi.org/10.1109/OJVT.2025.3631629.

[64] S. Yue, S. Zeng, L. Liu, Y. C. Eldar, B. Di, Hybrid Near-Far Field Channel Estimation for Holographic MIMO Communications, IEEE Transactions on Wireless Communications, Vol. 23, No. 11, 2024, pp. 15798–15813. https://doi.org/10.1109/TWC.2024.3433491.

[65] C. Girard, A. Dereux, Near-Field Optics Theories, Reports on Progress in Physics, Vol. 59, No. 5, 1996, pp. 657. https://doi.org/10.1109/ICCT62411.2024.1094632.

[66] L. Zakrajsek, E. Einarsson, N. Thawdar, M. Medley, J. M. Jornet, Design of Graphene-Based Plasmonic Nano-Antenna Arrays in the Presence of Mutual Coupling, in: 2017 11th European Conference on Antennas and Propagation (EUCAP), 2017, pp. 1381–1385. https://doi.org/10.1109/MCOM.2016.1600306CM.

[67] E. Bjoernson, Optimizing a Binary Intelligent Reflecting Surface for OFDM Communications under Mutual Coupling, in: WSA 2021; 25th International ITG Workshop on Smart Antennas, 2021, pp. 1–6.

[68] L. Dai, J. Tan, Z. Chen, H. V. Poor, Delay-Phase Precoding for Wideband THz Massive MIMO, IEEE Transactions on Wireless

Communications, Vol. 21, No. 9, 2022, pp. 7271–7286. https://doi.org/10.1109/TWC.2022.3157315.

[69] 5G; Study on Channel Model for Frequencies from 0.5 to 100 GHz (3GPP TR 38.901 version 19.2.0 Release 19), Technical Report TR 38.901 v19.2.0, ETSI / 3rd Generation Partnership Project (3GPP) RAN1 (Feb 2026).

[70] A. Kosasih, Ö. T. Demir, E. Björnson, Parametric Near-Field Channel Estimation for Extremely Large Aperture Arrays, in: 2023 57th Asilomar Conference on Signals, Systems, and Computers, 2023, pp. 162–166. https://doi.org/10.1109/IEEECONF59524.2023.10476971.

[71] W.-X. Long, M. Moretti, M. Morelli, L. Sanguinetti, R. Chen, Parametric Near-Field MMSE Channel Estimation for sub-THz XL-MIMO Systems, in: 2025 33rd European Signal Processing Conference (EUSIPCO), 2025, pp. 1198–1202. https://doi.org/10.48550/arXiv.2504.10064.

[72] C. Huang, J. Xu, W. Xu, X. You, C. Yuen, Y. Chen, Low-Complexity Channel Estimation for Extremely Large-Scale MIMO in Near Field, IEEE Wireless Communications Letters, Vol. 13, No. 3, 2024, pp. 671–675. https://doi.org/10.1109/LWC.2023.3339653.

[73] J. Kim, Y. Ahn, S. Kim, B. Shim, Deep Learning-Aided Parametric Sparse Channel Estimation for Terahertz Massive MIMO Systems, IEEE Transactions on Cognitive Communications and Networking, Vol. 10, No. 6, 2024, pp. 2136–2148. https://doi.org/10.1109/TCCN.2024.3401710.

[74] X. Zhang, J. Zheng, Non-Stationary Near-Field Channel Estimation for XL-MIMO Systems with Hybrid Combining, IEEE Wireless Communications Letters, Vol. 13, No. 10, 2024, pp. 2727–2731. https://doi.org/10.1109/LWC.2024.3442769.

[75] Z. Zhu, R. Yang, J. Zhang, S. Xu, C. Li, Y. Huang, L. Yang, Sparse Bayesian Learning-Based Adaptive Codebook for Near-Field Channel Estimation, in: ICC 2024 - IEEE International Conference on Communications, 2024, pp. 2366–2371. https://doi.org/10.1109/ICC51166.2024.10622416.

[76] H. Wang, K. Zhang, Q. Fu, F. Wen, X. Li, Enhanced Channel Estimation for Hybrid-Field XL-MIMO Systems Using Joint Sparse Bayesian Learning, IEEE Wireless Communications Letters, Vol. 14, No. 10, 2025, pp. 3099–3103. https://doi.org/10.1109/LWC.2025.3586299.

[77] H. Djelouat, M. Juntti, M. J. Sillanpää, B. D. Rao, Hybrid-Channel Estimation in Extra-Large MIMO Systems Via Regularized Sparse Bayesian Learning, in: 2025 33rd European Signal Processing Conference (EUSIPCO), 2025, pp. 1000–1004. https://doi.org/10.23919/EUSIPCO63237.2025.11226522.

[78] W. Xu, A. Liu, M.-j. Zhao, G. Caire, Joint Visibility Region Detection and Channel Estimation for XL-MIMO Systems via Alternating MAP, IEEE Transactions on Signal Processing, Vol. 72, 2024, pp. 4827–4842. https://doi.org/10.1109/TSP.2024.3479319.

[79] H. Wang, J. Fang, H. Duan, H. Li, L. Li, Near/Far-Field Channel Estimation for Terahertz Systems with ELAAs: A Block-Sparsity-Aware Approach, IEEE Transactions on Communications, Vol. 74, 2026, pp. 2685–2700.

[80] A. M. Elbir, K. Vijay Mishra, S. Chatzinotas, NBA-OMP: Near-Field Beam-Split-Aware Orthogonal Matching Pursuit for Wideband THz Channel Estimation, in: ICASSP 2023 - 2023 IEEE International Conference on Acoustics, Speech and Signal Processing (ICASSP), 2023, pp. 1–5.

[81] M. Cui, L. Dai, Near-Field Wideband Channel Estimation for Extremely Large-Scale MIMO, Science China Information Sciences, Vol. 66, No. 7, 2023, pp. 172303. https://doi.org/10.1007/s11432-022-3654-y.

[82] X. Guo, Y. Chen, Y. Wang, Compressed Channel Estimation for Near-Field XL-MIMO Using Triple Parametric Decomposition, IEEE Transactions on Vehicular Technology, Vol. 72, No. 11, 2023, pp. 15040–15045. https://doi.org/10.1109/TVT.2023.3279397.

[83] X. Zhang, H. Zhang, Y. C. Eldar, Near-Field Sparse Channel Representation and Estimation in 6G Wireless Communications, IEEE Transactions on Communications, Vol. 72, No. 1, 2024, pp. 450–464. https://doi.org/10.1109/TCOMM.2023.3322449.

[84] S. Liu, X. Yu, Z. Gao, J. Xu, D. W. K. Ng, S. Cui, Sensing-Enhanced Channel Estimation for Near-Field XL-MIMO Systems, IEEE Journal on Selected Areas in Communications, Vol. 43, No. 3, 2025, pp. 628–643. https://doi.org/10.1109/JSAC.2025.3531578.

[85] X. Zhang, Z. Wang, H. Zhang, L. Yang, Near-Field Channel Estimation for Extremely Large-Scale Array Communications: A Model-Based Deep Learning Approach, IEEE Communications Letters, Vol. 27, No. 4, 2023, pp. 1155–1159. https://doi.org/10.1109/LCOMM.2023.3245084.

[86] L. V. Nguyen, D. H. N. Nguyen, I. Atzeni, A. Tölli, A. L. Swindlehurst, Channel Estimation in Low-Resolution Near-Field Massive MIMO Systems, in: 2024 IEEE 13rd Sensor Array and Multichannel Signal Processing Workshop (SAM), 2024, pp. 1–5. https://doi.org/10.1109/SAM60225.2024.10636448.

[87] J. Gao, X. Chen, G. Y. LI, Deep Unfolding Based Channel Estimation for Wideband Terahertz Near-Field Massive MIMO Systems, Frontiers of Information Technology & Electronic Engineering, Vol. 25, No. 8, 2024, pp. 1162–1172.

https://doi.org/10.1631/FITEE.2300760.

[88] P. Zheng, X. Lyu, Y. Wang, Y. Gong, Channel Estimation for Wideband XL-MIMO: A Constrained Deep Unrolling Approach, IEEE Transactions on Wireless Communications, Vol. 25, 2026, pp. 8018–8031. https://doi.org/10.1109/TWC.2025.3635198.

[89] S. Gao, P. Dong, Z. Pan, X. You, Lightweight Deep Learning Based Channel Estimation for Extremely Large-Scale Massive MIMO Systems, IEEE Transactions on Vehicular Technology, Vol. 73, No. 7, 2024, pp. 10750–10754. https://doi.org/10.1109/TVT.2024.3364510.

[90] W. Yu, Y. Shen, H. He, X. Yu, J. Zhang, K. B. Letaief, Hybrid Far- and Near-Field Channel Estimation for THz Ultra-Massive MIMO via Fixed Point Networks, in: GLOBECOM 2022 - 2022 IEEE Global Communications Conference, 2022, pp. 5384–5389. https://doi.org/10.48550/arXiv.2205.04944.

[91] H. Lei, J. Zhang, H. Xiao, X. Zhang, B. Ai, D. W. K. Ng, Channel Estimation for XL-MIMO Systems with Polar-Domain Multi-Scale Residual Dense Network, IEEE Transactions on Vehicular Technology, Vol. 73, No. 1, 2024, pp. 1479–1484. https://doi.org/10.48550/arXiv.2308.16400.

[92] Z. Jin, L. You, D. Wing Kwan Ng, X.-G. Xia, X. Gao, Near-Field Channel Estimation for XL-MIMO: A Deep Generative Model Guided by Side Information, IEEE Transactions on Cognitive Communications and Networking, Vol. 12, 2026, pp. 628–643. https://doi.org/10.48550/arXiv.2505.06900.

[93] M. Ye, X. Liang, C. Pan, Y. Xu, M. Jiang, C. Li, GAN-Based Near-Field Channel Estimation for Extremely Large-Scale MIMO Systems, IEEE Transactions on Green Communications and Networking, Vol. 9, No. 1, 2025, pp. 304–316. https://doi.org/10.1109/TGCN.2024.3416617.

[94] R. Schmidt, Multiple Emitter Location and Signal Parameter Estimation, IEEE Transactions on Antennas and Propagation, Vol. 34, No. 3, 1986, pp. 276–280. https://doi.org/10.1109/TAP.1986.1143830.

[95] H. Trees, Optimum Array Processing, John Wiley & Sons, Ltd, 2002.

[96] W.-X. Long, S. Ye, M. Moretti, M. Morelli, L. Sanguinetti, R. Chen, C.-X. Wang, Channel Estimation for 6G Near-Field Wireless Communications: A Comprehensive Survey, IEEE Communications Surveys Tutorials, Vol. 28, 2026, pp. 5496–5531. https://doi.org/10.1109/COMST.2026.3676861.

[97] X. Guo, Y. Chen, Y. Wang, C. Yuen, Exploiting Structured Sparsity in Near Field: From the Perspective of Decomposition, IEEE Communications Magazine, Vol. 63, No. 1, 2025, pp. 37–43. https://doi.org/10.1109/MCOM.001.2300836.

[98] A. Jagannath, J. Jagannath, T. Melodia, Redefining Wireless Communication for 6G: Signal Processing Meets Deep Learning with Deep Unfolding, IEEE Transactions on Artificial Intelligence, Vol. 2, No. 6, 2021, pp. 528–536. https://doi.org/10.1109/TAI.2021.3108129.

[99] I. Daubechies, M. Defrise, C. De Mol, An Iterative Thresholding Algorithm for Linear Inverse Problems with a Sparsity Constraint, Communications on Pure and Applied Mathematics: A Journal Issued by the Courant Institute of Mathematical Sciences, Vol. 57, No. 11, 2004, pp. 1413–1457. https://doi.org/10.1002/cpa.20042.

[100] K. Gregor, Y. LeCun, Learning Fast Approximations of Sparse Coding, in: Proceedings of the 27th International Conference on International Conference on Machine Learning, ICML'10, Omnipress, Madison, WI, USA, 2010, p. 399–406.

[101] R. Chen, Y. Sun, T. Liu, X. Li, Z. Wang, Research on Channel Estimation Technique Based on Convolutional Neural Network, in: 2025 10th International Conference on Intelligent Computing and Signal Processing (ICSP), 2025, pp. 186–189. https://doi.org/10.1109/ICSP65755.2025.11087146.

[102] Y. Jin, J. Zhang, C. Huang, L. Yang, H. Xiao, B. Ai, Z. Wang, Multiple Residual Dense Networks for Reconfigurable Intelligent Surfaces Cascaded Channel Estimation, IEEE Transactions on Vehicular Technology, Vol. 71, No. 2, 2022, pp. 2134–2139. https://doi.org/10.1109/TVT.2021.3132305.

[103] D. Tse, P. Viswanath, Fundamentals of Wireless Communication, Cambridge University Press, USA, 2005. https://doi.org/10.1017/CBO9780511807213.

[104] Z. Zhang, Y. Liu, Z. Wang, X. Mu, J. Chen, Physical Layer Security in Near-Field Communications, IEEE Transactions on Vehicular Technology, Vol. 73, No. 7, 2024, pp. 10761–10766. https://doi.org/10.1109/TVT.2024.3366115.

[105] J. Tian, Y. Han, Z. Jin, X. Yang, J. Yang, W. Tang, X. Li, W. Wang, S. Jin, Pioneering Scalable Prototype for Mid-Band XL-MIMO Systems: Design and Implementation, IEEE Journal on Selected Areas in Communications, Vol. 44, 2026, pp. 3365–3381. https://doi.org/10.1109/JSAC.2026.3656471.

[106] W. Fan, Z. Yuan, Y. Lyu, J. Zhang, J. Borrill, F. Zhang, Near-Field Channel Characterization for Midband ELAA Systems: Sounding, Parameter Estimation, and Modeling, IEEE Vehicular Technology Magazine, Vol. 20, No. 3, 2025, pp. 87–96. https://doi.org/10.1109/MVT.2025.3565848.

[107] M. Mora, Y. Gong, R. Morawski, T. Le-Ngoc, Experimental Studies of Near-Field Beamfocusing with Extra-Large Antenna Array Prototype, in: IEEE 36th International Symposium on Personal, Indoor and Mobile

Radio Communications (PIMRC), 2025, pp. 1–6. https://doi.org/10.1109/PIMRC62392.2025.11274928.

[108] J. An, C. Xu, D. W. K. Ng, G. C. Alexandropoulos, C. Huang, C. Yuen, L. Hanzo, Stacked Intelligent Metasurfaces for Efficient Holographic MIMO Communications in 6G, IEEE Journal on Selected Areas in Communications, Vol. 41, No. 8, 2023, pp. 2380–2396. https://doi.org/10.1109/JSAC.2023.3288261.

[109] J. Zhu, V. Y. F. Tan, L. Dai, MIMO Capacity Analysis and Channel Estimation for Electromagnetic Information Theory, IEEE Journal on Selected Areas in Communications, Vol. 44, 2026, pp. 3302–3316. https://doi.org/10.1109/JSAC.2026.3654525.

[110] Z. Xie, Y. Liu, J. Xu, X. Wu, A. Nallanathan, Performance Analysis for Near-Field MIMO: Discrete and Continuous Aperture Antennas, IEEE Wireless Communications Letters, Vol. 12, No. 12, 2023, pp. 2258–2262. https://doi.org/10.1109/LWC.2023.3317492.

[111] J. Zhu, Z. Wan, L. Dai, T. Jun Cui, Electromagnetic Information Theory-Based Statistical Channel Model for Improved Channel Estimation, IEEE Transactions on Information Theory, Vol. 71, No. 3, 2025, pp. 1777–1793. https://doi.org/10.1109/TIT.2025.3526689.

[112] J. Zhu, Z. Wan, L. Dai, M. Debbah, H. V. Poor, Electromagnetic Information Theory: Fundamentals, Modeling, Applications, and Open Problems, IEEE Wireless Communications, Vol. 31, No. 3, 2024, pp. 156–162. https://doi.org/10.1109/MWC.019.2200602.

[113] Q. Dai, Y. Zeng, H. Wang, C. You, C. Zhou, H. Cheng, X. Xu, S. Jin, A. Lee Swindlehurst, Y. C. Eldar, R. Schober, R. Zhang, X. You, A Tutorial on MIMO-OFDM ISAC: From Far-Field to Near-Field, IEEE Communications Surveys & Tutorials, Vol. 28, 2026, pp. 4319–4358. https://doi.org/10.1109/COMST.2025.3650568.

[114] H. Chen, M. F. Keskin, A. Sakhnini, N. Decarli, S. Pollin, D. Dardari, H. Wymeersch, 6G Localization and Sensing in the Near Field: Features, Opportunities, and Challenges, IEEE Wireless Communications, Vol. 31, No. 4, 2024, pp. 260–267. https://doi.org/10.1109/MWC.011.2300359.

[115] H. Lei, J. Zhang, Z. Wang, B. Ai, E. Björnson, Near-Field User Localization and Channel Estimation for XL-MIMO Systems: Fundamentals, Recent Advances, and Outlooks, IEEE Wireless Communications, Vol. 32, No. 4, 2025, pp. 190–198. https://doi.org/10.1109/MWC.010.2400237.

[116] X. Luo, J. Du, Y. Chen, J. Zhang, X. Li, F. Gao, Tensor-Based Framework for Multi-User RIS-Assisted ISAC in Cross Far- and Near-Field Communications, IEEE Transactions on Wireless Communications, Vol. 25, 2026, pp. 5339–5354. https://doi.org/10.1109/TWC.2025.3617773.

[117] F. Ciampa, M. Meo, E. Barbieri, Impact Localization in Composite Structures of Arbitrary Cross Section, Structural Health Monitoring, Vol. 11, No. 6, 2012, pp. 643–655. https://doi.org/10.1177/1475921712451951.

[118] J. He, M. O. Ahmad, M. N. S. Swamy, Near-Field Localization of Partially Polarized Sources with a Cross-Dipole Array, IEEE Transactions on Aerospace and Electronic Systems, Vol. 49, No. 2, 2013, pp. 857–870. https://doi.org/10.1109/TAES.2013.6494385.

[119] X. Wu, W.-P. Zhu, Single Far-Field or Near-Field Source Localization with Sparse or Uniform Cross Array, IEEE Transactions on Vehicular Technology, Vol. 69, No. 8, 2020, pp. 9135–9139. https://doi.org/10.1109/TVT.2020.2998128.

[120] X. Wu, J. Yan, 3-D Mixed Far-Field and Near-Field Sources Localization with Cross Array, IEEE Transactions on Vehicular Technology, Vol. 69, No. 6, 2020, pp. 6833–6837. https://doi.org/10.1109/TVT.2020.2985903.

[121] D. Xue, Y. Guo, L. Yu, J. Huo, H. Chen, W. Liu, Three-Dimensional Near-Field Localization with Cross Array Considering Amplitude Attenuation, Circuits, Systems, and Signal Processing, Vol. 42, 2023, pp. 1–14. https://doi.org/10.1007/s00034-023-02295-5.

[122] H. Friis, A Note on a Simple Transmission Formula, Proceedings of the IRE, Vol. 34, No. 5, 1946, pp. 254–256. https://doi.org/10.1109/JRPROC.1946.234568.